Examination of the Pore Space of a Solid Oxide Fuel Cell Electrode: A Computational Approach

by

Drew Blore

A thesis submitted to the
Department of Mechanical and Materials Engineering
in conformity with the requirements for
the degree of Master of Applied Science

Queen's University
Kingston, Ontario, Canada
June 2011

Abstract

A numerical model of a solid oxide fuel cell electrode is presented. Using an already established algorithm for dropping spheres as a base, alterations are made to the algorithm to increase the realism of the model. Two changes are analyzed in detail: the ability to drop pore former particles, and the use of pre-agglomerated solid particles. These changes are characterized by their impact on mean pore size, tortuosity, and effective diffusivity. As pore former volume fraction is increased, so too are mean pore size and tortuosity. A higher mean pore size has a beneficial effect on effective diffusivity due to Knudsen effects, while a higher tortuosity has a detrimental effect on effective diffusivity. The impact of mean pore size and tortuosity on diffusivity generally balances and if the impact of porosity is ignored, pore former volume fraction does not greatly affect effective diffusivity. As pore former particle size is increased, mean pore size and tortuosity also increase. Similarly to before, the effects of mean pore size and tortuosity balance. However, effective diffusivity is shown to decrease slightly with an increasing pore former particle size, suggesting a change in tortuosity has greater impact on diffusivity than a change in mean pore size. For a domain constructed with pre-agglomerated particles, the tortuosity and mean pore size were both noticeably larger than when no pre-agglomerated particles are used. Effective diffusivity was only slightly higher for a domain constructed with pre-agglomerated particles than with no pre-agglomerated particles. It is also shown that the relationship of effective diffusivity with porosity for a domain constructed with pre-agglomerated particles does not fit the correlation proposed by Berson et al. [1] for low porosity structures.

A secondary goal of this work is to examine pore size measurement techniques, and present a novel technique that allows the determination of a local pore size, and therefore, a local Knudsen number. Results from the local pore size technique do not match those of the random walk method and so although the novel technique may prove to be a good starting point, it is deemed not yet suitable for use.

Acknowledgments

I would like to thank my supervisor, Dr. Jon Pharoah, for his ideas and support throughout the research and writing process. I would also like to thank Dr. Steven Beale from the National Research Council of Canada for providing advice during the research for this work. I would like to thank everybody at the Fuel Cell Research Centre (FCRC) in Kingston, ON for providing an excellent facility to research and work in. Especially of note are Dr. Arganthael Berson and Dr. Hai Won Choi for providing help and guidance nearly every day of working at the FCRC. I would also like to thank all of the professors and administrative personnel in the Department of Mechanical Engineering at Queen's University in Kingston, ON. For their financial support during this work I would like to thank Ontario Graduate Scholarships (OGS). Finally, a very special thanks goes out to my friends and family for their support, encouragement, and patience during the time I spent working on this thesis.

Nomenclature

a	activity
c^*	surface concentration
D	self diffusion coefficient
D_{bulk} or Db	diffusivity in open space
D_{eff} or De	effective diffusivity
d	characteristic length
E	open circuit potential
E^0	open circuit potential at standard conditions
E_T	open circuit potential at temperature T
F	Faraday's constant
f	decay rate
$\Delta\hat{g}$	Gibbs free energy
$\Delta\hat{g}_{rxn}$	free energy change of reaction
$\Delta\hat{g}^0_{rxn}$	standard state free energy change of reaction
$\Delta G_1^{\ddagger}$	activation barrier of forward reaction
$\Delta\hat{h}_{HHV}$	enthalpy using higher heating value
i	current
j	current density
j_0	exchange current density
j_L	limiting current density
Kn	Knudsen number
l	chord length
n	number of electrons in reaction
P	power
R	universal gas constant
R_{elec}/R_{ionic}	resistance

$\Delta\hat{s}$	entropy change
s	distance
T	temperature
T_0	temperature at standard conditions
t	time
V	voltage
v_T	thermal velocity

Greek

α	activation barrier transfer coefficient
β	wall collision model coefficient
ϵ	efficiency
ε	porosity
η	overvoltage
γ_{1j}	angle between 1st chord and jth chord
λ	molecular free path
ϕ	density of diffusing gas
τ	tortuosity
υ_{fuel}	rate of fuel supply
υ_i	stoichiometric coefficient
ξ	particle displacement

Contents

Abstract i

Acknowledgments iii

Nomenclature iv

Contents vi

List of Tables viii

List of Figures ix

Chapter 1: Introduction 1
- 1.1 Motivation . . . 1
- 1.2 Background Information . . . 3
  - 1.2.1 SOFC Fundamentals . . . 3
  - 1.2.2 SOFC Thermodynamics . . . 7
  - 1.2.3 Fuel Cell Losses . . . 8
  - 1.2.4 SOFC Electrodes . . . 12
  - 1.2.5 CFD Modeling . . . 16
- 1.3 Scope . . . 17
- 1.4 Organization of Thesis . . . 18

Chapter 2: Literature Review 20
- 2.1 SOFC Electrodes . . . 20
  - 2.1.1 Electrode Fabrication . . . 20
  - 2.1.2 Electrode Characterization . . . 21
- 2.2 Micro-modeling . . . 24
- 2.3 Pore Size Analysis . . . 25

Chapter 3: Modeling Techniques 28
- 3.1 Existing Model . . . 28

3.2 Improvements to Existing Model 30
3.2.1 Addition of Pore Former 31
3.2.2 Agglomerated Particles 31
3.3 Solving Diffusivity 33
3.3.1 Random Walk Simulations 34
3.3.2 Finite Volume Method Simulations 35

Chapter 4: Pore Size Measurement and Analysis **39**
4.1 Pore Size Measurement Methods 39
4.1.1 Mercury Intrusion Porosimetry 39
4.1.2 Sphere Growth Methods 40
4.1.3 Chord Length Methods 41
4.2 Local Knudsen Effects 43
4.2.1 Measuring Local Pore Size 44
4.2.2 Comparison to Random Walk Method 45

Chapter 5: Characterization of New Features **49**
5.1 Pore Former Particles 49
5.1.1 Effect of Altering Pore Former Volume Fraction 50
5.1.2 Effect of Altering Pore Former Particle Size 62
5.2 Dropping Solid Agglomerates 71
5.2.1 Pore Size Distribution 72
5.2.2 Tortuosity 75
5.2.3 Effective Diffusivity 77

Chapter 6: Summary and Conclusions **81**
6.1 Summary 81
6.2 Conclusion 82
6.3 Future Work 83

Bibliography **85**

Appendix A: Additional Figures **91**

Appendix B: Additional Analysis **96**
B.1 FVM Diffusivity Results 96

List of Tables

B.1 Effective diffusivity for several values of pore former volume fraction using FVM. 96

B.2 Effective diffusivity for several values of pore former particle size using FVM. 96

B.3 Effective diffusivity for a varying number of pre-agglomerated phases using FVM. 96

List of Figures

1.1 Schematic of solid oxide fuel cell. 3

1.2 Schematic of solid oxide fuel cell with electrochemical equations. . . . 5

1.3 A typical fuel cell polarization curve 5

1.4 Cross-sectional view of the SOFC microstructure. 13

2.1 3D image of an SOFC electrode reconstructed using FIB-SEM technology 22

2.2 Various methods of characterizing pore size compared to the Bosanquet correlation. 27

3.1 Geometrical relationship of two overlapping spheres 30

3.2 Drawing of the four particle agglomerate. 33

3.3 Steps to create a snappyHexMesh on a 2D domain. 37

4.1 Relationship between mean pore size and volume fraction of pore former using a structured measurement. 46

4.2 $\langle l^2 \rangle / 2 \langle l \rangle^2$ as a function of pore former volume fraction. 47

5.1 3D model of a $10\mu m \times 10\mu m \times 10\mu m$ section of SOFC electrode with constant porosity. 51

5.2 3D model of a $10\mu m \times 10\mu m \times 10\mu m$ section of SOFC electrode with constant particle overlap. 52

5.3 Relationship between mean pore size and volume fraction of pore former. 53
5.4 Chord length distribution for three different quantities of pore former volume fraction. 55
5.5 2-dimensional slices of the 3D electrode model with varying pore former volume fraction. 57
5.6 Variation of effective diffusivity as a function of pore former volume fraction. 58
5.7 Effective diffusivity, De/Db, normalized to the expected theoretical result. 59
5.8 Graphical representation of the Bosanquet correlation. 60
5.9 Effective diffusivity, De/Db, normalized to the expected theoretical result for a realistically sized electrode. 61
5.10 3D model of a $10\mu m \times 10\mu m \times 10\mu m$ section of SOFC electrode created with different sizes of pore former particles. 63
5.11 Relationship between mean pore size and pore former particle diameter. 64
5.12 Chord length distribution for domains constructed with 3 different pore former particle diameters. 66
5.13 $\langle l^2 \rangle / 2\langle l \rangle^2$ as a function of pore former particle size. 67
5.14 2-dimensional slices of the 3D electrode model with varying pore former particle size. 69
5.15 Variation of effective diffusivity as a function of pore former particle size. 70
5.16 Variation of effective diffusivity as a function of pore former particle size for a realistically sized geometry. 71
5.17 3D model of a $10\mu m \times 10\mu m \times 10\mu m$ section of SOFC electrode. . . . 73

5.18 Relationship between mean pore size and porosity of a domain created with Agglomerates 74
5.19 Chord length distribution for the three cases of this study. 75
5.20 2-dimensional slices of the 3D electrode model with both the old single sphere algorithm and the new pre-agglomerated particle algorithm. . 76
5.21 Diffusivity as a function of porosity for various levels of pre-agglomerated particle use. 79
5.22 Diffusivity normalized to $1.6\varepsilon^2$ as a function of porosity for a realistically sized electrode with pre-agglomerated particles. 80

A.1 Extra 2-dimensional slices of the 3D electrode model with varying pore former volume fraction. 92
A.2 Extra 2-dimensional slices of the 3D electrode model with varying pore former volume fraction and constant particle overlap. 93
A.3 Extra 2-dimensional slices of the 3D electrode model with varying pore former particle size. 94
A.4 Extra 2-dimensional slices of the 3D electrode model with various levels of pre-agglomeration. 95

Chapter 1

Introduction

1.1 Motivation

As fossil fuel reserves are depleted around the world, the need for alternative and renewable energy sources has grown considerably. Additionally, this need is even more important as the effects of global warming are felt around the world. Popular alternative energy sources include nuclear, chemical, hydro, wind, solar, tidal, and biofuel. Fuel cells are not an energy source, but rather an energy conversion device that produces electricity from chemical potential energy. To be competitive with both conventional fossil fuel methods as well as other alternative energy methods, fuel cell research must continue to grow. Fuel cells have a number of distinct advantages over these other energy technologies. Fuel cells produce electricity directly from chemical energy, which means they are typically far more efficient than combustion engines [2]. Fuel cells also rarely have any moving parts and are therefore not subject to mechanical losses. Unlike batteries, fuel cells scale well to large (1MW) and small sizes (1W) and can also be quickly refueled, whereas a battery must be replaced or slowly recharged. The ability to produce fuel cells in many different sizes makes them incredibly versatile and applicable to both portable and stationary power applications. Of course, the greatest advantage of a fuel cell is its ability to produce zero greenhouse gas emissions when hydrogen is used as a fuel.

A Solid Oxide Fuel Cell (SOFC), displayed in Figure 1.1, is a high temperature fuel cell suitable for stationary applications. Arguably, the most important components of an SOFC are the electrodes since gas, electrons, and ions all must be transported effectively. As well, with the advance of composite electrodes in SOFCs, many electrochemical reactions occur within the electrode itself and not just at the electrode-electrolyte interface. Improvement of transport in the electrodes is key to improvement in SOFC performance. 3D image processing techniques (FIB-SEM, XCT) are a popular way to characterize porous electrodes. However, these techniques are costly and require an actual fuel cell electrode to be manufactured before any computational simulations can be performed. Alternatively, a common computational model of an electrode uses randomly packed spheres to mimic the solid phases of the porous electrode. These models are advantageous in that they are quick to make, allow parametric studies to be performed, and can build theoretic geometries which may be impossible to manufacture with current technology. However, random sphere models are sometimes viewed as too simplistic because real electrode particles are often non-spherical shapes. Improvement of the basic randomly packed spheres model could allow an actual fuel cell electrode to be captured computationally with greater accuracy.

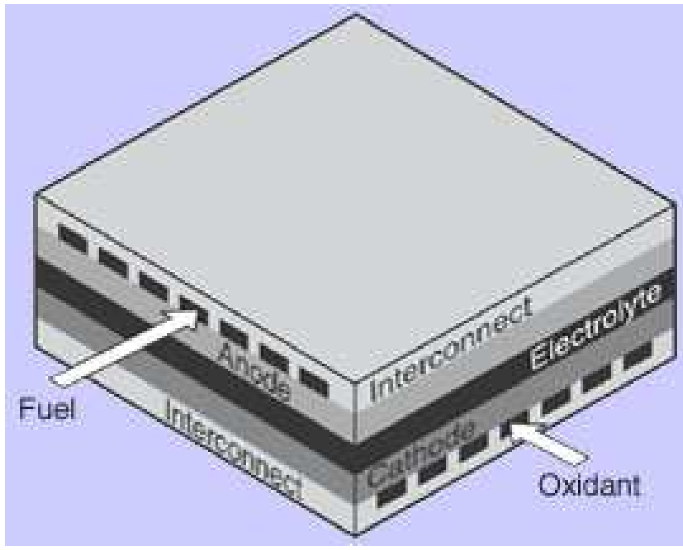

Figure 1.1: Schematic of solid oxide fuel cell.[3]

1.2 Background Information

The primary sources for background information in this section are: Fuel Cell Fundamentals [2], which provides an excellent overview of all fuel cells, and High Temperature Solid Oxide Fuel Cells [4], which provides detailed information on SOFCs.

1.2.1 SOFC Fundamentals

All types of fuel cells operate in the same basic way. Similarly to a battery, a fuel cell consists of two porous electrodes - the anode and the cathode. An oxidation reaction occurs at the anode while an oxygen reduction reaction occurs at the cathode. Ions are transferred between the two electrodes via an electrolyte. Electrons are transferred between the electrodes (and also through the load) via an interconnect system.

A solid oxide fuel cell (SOFC) is named as such due to the electrolyte being made of a non-porous solid oxide ceramic material. The most widely used SOFC electrolyte is Yttria-Stabilised Zirconia (YSZ). In all types of fuel cells, the electrons flow from the anode to the cathode. In an SOFC, O^{2-} ions are transferred from the cathode to the anode. In some other types of fuel cells (such as the PEMFC), ions are transferred in the opposite direction - anode to cathode. Before the O^{2-} ions can travel across the electrolyte they must first be created at the cathode. O_2 molecules from the air flow channel react with electrons coming from the interconnect. The oxygen reduction reaction for a hydrogen fuel cell is:

$$\frac{1}{2}O_2 + 2e^- \rightarrow O^{2-} \tag{1.1}$$

This reaction must take place where electrons, ions, and gas molecules (in this case O_2) exist together. This region is known as the triple phase boundary (TPB) and is named such because it is where the electron transporting phase, ion transporting phase, and pore phase all meet. When O^{2-} ions reach the anode, they will once again react at a TPB; though this time it is with the fuel. The oxidation reaction of a hydrogen fuel cell is:

$$H_2 + O^{2-} \rightarrow H_2O + 2e^- \tag{1.2}$$

This reaction produces H_2O molecules that are transported back through the electrode and released out the flow channel as exhaust, and electrons which flow into the wire interconnect. A schematic of an SOFC is depicted in Figure 1.2 [4].

A polarization curve shows how the voltage of a device is affected as current density changes. A polarization curve is a common way to characterize the performance of a fuel cell. Figure 1.3 is an example of a typical polarization curve for a fuel cell. The

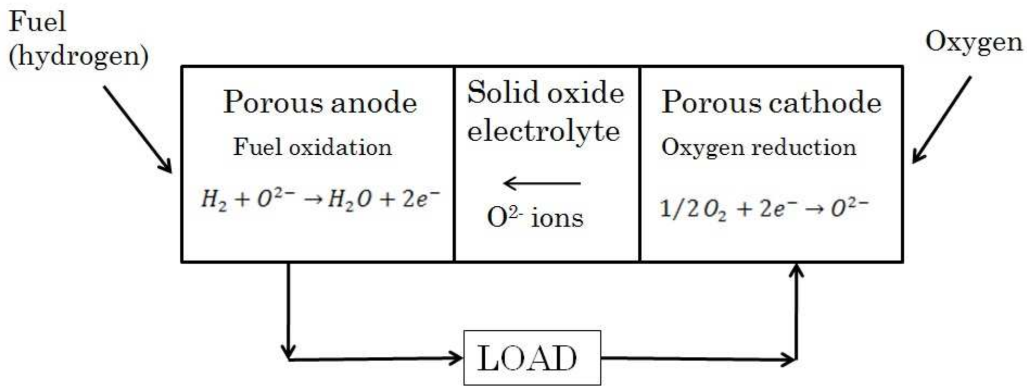

Figure 1.2: Schematic of solid oxide fuel cell with electrochemical equations.

power (P) delivered by a fuel cell is equal to the product of the voltage (V) and the current (i):

$$P = iV \tag{1.3}$$

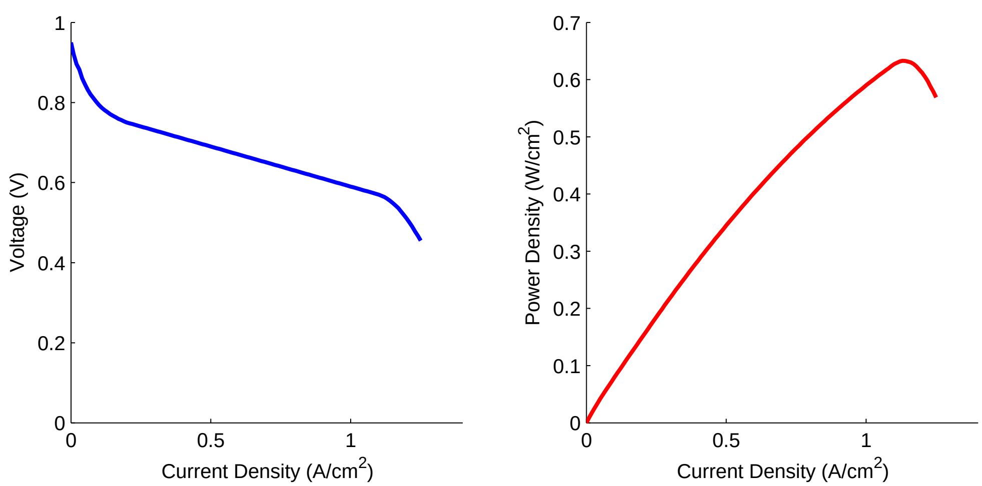

Figure 1.3: A typical fuel cell polarization curve and power density curve

The current of a fuel cell is directly proportional to the fuel consumed in the cell.

Consequently, as the voltage of the fuel cell decreases, the electric power per unit of fuel also decreases. Therefore, efficiency is directly proportional to cell voltage [2]. Under a current load there are irreversible losses that lower the voltage output of the fuel cell. These losses become greater as more current is drawn from the cell. There are 3 major losses in a hydrogen fuel cell:

- Activation losses
- Ohmic losses
- Concentration losses

The true voltage output (V) of a fuel cell is determined by:

$$V = E - \eta_{act} - \eta_{ohm} - \eta_{con} \tag{1.4}$$

Where E is the open circuit voltage determined by thermodynamics, η_{act} is activation losses due to reaction kinetics, η_{ohm} is ohmic losses from electronic and ionic conduction, and η_{con} is concentration losses due to mass transport.

The real efficiency of a fuel cell must take into account the reversible thermodynamic efficiency ε_{thermo}, the voltage efficiency $\varepsilon_{voltage}$, and the fuel utilization efficiency ε_{fuel}. The real efficiency (ε_{real}) of a cell is then defined as:

$$\epsilon_{real} = \left(\frac{\Delta\hat{g}}{\Delta\hat{h}_{HHV}}\right)\left(\frac{V}{E}\right)\left(\frac{i/nF}{\upsilon_{fuel}}\right) \tag{1.5}$$

Where the reversible thermodynamic efficiency contains Gibbs Free Energy ($\Delta\hat{g}$), and enthalpy of reaction using the higher heating value ($\Delta\hat{h}_{HHV}$). The voltage efficiency contains the real operating voltage of the fuel cell (V), and the thermodynamically reversible voltage of the fuel cell (E). Finally, the fuel utilization efficiency consists of the current generated by the fuel cell (i), the number of electrons transferred in the reaction (n), Faraday's Constant (F), and the rate at which fuel is supplied to the fuel cell (υ_{fuel}) in mol/sec.

1.2.2 SOFC Thermodynamics

The reversible voltage of a hydrogen fuel cell under standard-state conditions is:

$$E^0 = -\frac{\Delta\hat{g}^0_{rxn}}{nF} \tag{1.6}$$

Where $\Delta\hat{g}^0_{rxn}$ is the standard-state free energy change for a reaction.

However, SOFCs rarely operate at standard-state conditions, so the effects of temperature, pressure, and concentration must also be accounted for. To account for temperature, E_T represents the reversible cell voltage at an arbitrary temperature, T, and is defined as:

$$E_T = E^0 + \frac{\Delta\hat{s}}{nF}(T - T_0) \tag{1.7}$$

Where $\Delta\hat{s}$ is the entropy change of the reaction, and T_0 is the temperature at standard-state conditions (at which E^0 is calculated).

Now to account for pressure and concentration, the Nernst equation is introduced:

$$E = E^0 - \frac{RT}{nF}\ln\frac{\Pi a^{\upsilon_i}_{products}}{\Pi a^{\upsilon_i}_{reactants}} \tag{1.8}$$

Where E is the reversible cell voltage, R is the universal gas constant, a is the activity of a specific species, and υ_i is the stoichiometric coefficient of a specific species. The combination of equations 1.7 and 1.8 allow the reversible voltage of a fuel cell to be calculated under any set of conditions. A modified Nernst equation that takes temperature into account is then:

$$E = E_T - \frac{RT}{nF} \ln \frac{\Pi a_{products}^{v_i}}{\Pi a_{reactants}^{v_i}} \tag{1.9}$$

1.2.3 Fuel Cell Losses

Activation Losses

A fuel cell reaction involves the transfer of electrons between a surface and a chemical species. The kinetics of an electrochemical reaction represents the mechanisms by which electron transfer occurs. The current produced by a fuel cell depends on the rate of the reactions. Therefore, it is important to increase the rate of electrochemical reaction to improve overall fuel cell performance.

The activation overvoltage, n_{act}, represents the voltage lost due to the performance of the reaction kinetics. The anode and the cathode both have separate activation overvoltages, $n_{act,a}$ and $n_{act,c}$ respectively, that contribute to the total activation overvoltage. When H_2 is used as a fuel, $n_{act,c}$ is by far the dominant contributor to the total n_{act}. However when H_2 is not used as a fuel, which is often the case in SOFCs, the importance of $n_{act,a}$ can become just as significant as $n_{act,c}$.

Current density, j, is related to the reaction rate by $j = nFv$, where v is the reaction rate per unit-area. Since reactions take place in both forward and reverse directions, there is a forward and reverse current density. The forward current density is expressed as:

$$j_1 = nFc_R^* f_1 e^{-\Delta G_1^{\ddagger}/(RT)} \tag{1.10}$$

The reverse current density is then given by:

$$j_2 = nFc_P^* f_2 e^{-(\Delta G_1^{\ddagger} - \Delta G_{rxn})/(RT)} \tag{1.11}$$

Where c^* is the surface concentration of either the reactant or product. f_1 and f_2 are the decay rates from reactant to product and from product to reactant respectively. $-\Delta G_1^{\ddagger}$ is the activation barrier for the forward reaction. ΔG_{rxn} is the difference between the forward reaction activation barrier and the reverse reaction activation barrier. At thermodynamic equilibrium, the forward and reverse current densities must be equal. In this state, the current density is known as the exchange current density, j_0.

The Bulter-Volmer equation represents the net current density of a fuel cell ($j_1 - j_2$). The equation contains n_{act}, which allows the determination of the activation overvoltage at any current density. If the concentration dependence of the exchange current density is taken into account, the Bulter-Volmer equation is expressed as:

$$j = j_0^0 \left(\frac{c_R^*}{c_R^{0*}} e^{\alpha n F \eta/(RT)} - \frac{c_P^*}{c_P^{0*}} e^{-(1-\alpha) n F \eta/(RT)} \right) \tag{1.12}$$

Where η is the activation voltage loss, and α is the transfer coefficient of the activation barrier. j_0^0 is the exchange current density measured at the reference reactant and product concentration values c_R^{0*} and c_P^{0*}. c_R^* and c_P^* are the actual surface concentrations of the rate-limiting species in the reaction.

Ohmic Losses

Not only must current be generated by electrochemical reactions, it also must be transported across the fuel cell. Two types of charged particles - electrons and ions

- are transported within a fuel cell. In most cases, ion charge transport is more difficult than electron transport due to the ion's comparatively large mass. The internal resistance of a fuel cell to electron and ion transport causes a voltage loss, n_{ohm}.

Voltage loss due to charge transport obeys ohm's law, hence the name ohmic loss. Including both the electronic and ionic resistances, n_{ohm} is expressed as:

$$\eta_{ohmic} = i(R_{elec} + R_{ionic}) \tag{1.13}$$

Concentration Losses

Mass transport in a fuel cell involves the movement of reactants and products to and from the electrode-electrolyte interface. As seen in the previous section, charge transport is moved by conduction; mass transport however, is moved by diffusion and convection. Reactant and product concentrations at the electrode-catalyst interface are what determines fuel cell performance. Any decrease in concentration between the fuel cell inlet and the catalyst layer will cause a reduction in performance called the mass transport loss. Mass transport in a fuel cell can be split into two parts: transport in the fuel cell electrode which is dominated by diffusion, and transport in the fuel cell flow channel which is dominated by convection.

On one side of an electrode is the electrolyte; while on the other side is the flow channel. Due to electrochemical reactions at the electrode-electrolyte interface, reactant becomes depleted and a concentration gradient is developed and reactant is moved from flow channel to electrolyte. Likewise, as product is created at the electrode-electrolyte interface, another concentration gradient moves the product from electrolyte to flow channel. This difference in concentration between the flow channel and the electrolyte causes losses in the thermodynamics (Nernstian losses), and losses in the kinetics (reaction losses). These losses are evident by inspecting how concentration affects both the Nernst equation (1.9) and the Butler-Volmer equation (1.12). Combining these factors into one equation yields:

$$\eta_{conc} = c \ln \frac{j_L}{j_L - j} \tag{1.14}$$

Where c is a constant of the form:

$$c = \frac{RT}{nF}\left(1 + \frac{1}{\alpha}\right) \tag{1.15}$$

j_L is known as the limiting current density. As current density rises, reactant concentration at the catalyst layer decreases. The limiting current density represents the current density at which catalyst layer reactant concentration drops to zero.

In any fuel cell, losses can also occur from poor flow distribution in the fuel cell flow plate (or interconnect in SOFCs). If the flow travels through the channel too fast, little of the reactant will diffuse through the electrode. Also, reactant must be effectively distributed across the entire electrode area, while all product must be carried out of the fuel cell through the flow channel. In SOFCs, the interconnect is made from metals or ceramics such as lanthanum chromite. Stability and durability of the flow plate are very important due to the high temperatures of SOFCs, which facilitates degradation. Thermal properties of the flow plate must match those of the rest of the fuel cell to avoid mechanical stress issues due to thermal expansion.

1.2.4 SOFC Electrodes

An SOFC electrode is made of a particulate solid that is sintered to form a porous conducting layer. Nickel is the main material used in anodes due to its known performance, cost, and availability. In cathodes, lanthanum manganites represent the most used materials since 1973, most notably LSM. In both electrode types, the material must be porous enough to provide adequate diffusivity, while also maintaining an appropriate level of electronic and ionic conductivity [4]. The microstructural characteristics of an electrode not only depend on the materials used, but also the method of fabrication. Various fabrication methods are analyzed in section 2.1. Figure 1.4 displays a scanning electron microscope (SEM) picture of an SOFC microstructure. Five different layers are shown along with their thicknesses: cathode support layer, cathode active layer, electrolyte, anode active layer, and anode support layer (substrate).

To achieve a desired porosity within an electrode, pore former is often used. Pore former particles are often made of carbon or acrylic and are mixed in with the electrode material as a slurry or an ink. After application of the slurry or ink, the pore former phase is evaporated under high temperatures during the sintering process. With the pore former phase gone, additional pore space is created and a higher porosity is achieved.

Cathode

Cathodes in SOFCs must have many properties including high electrical conductivity, high catalytic activity for the oxygen reduction reaction, and similar thermal expansion properties to the other fuel cell components. In early SOFCs, platinum was used

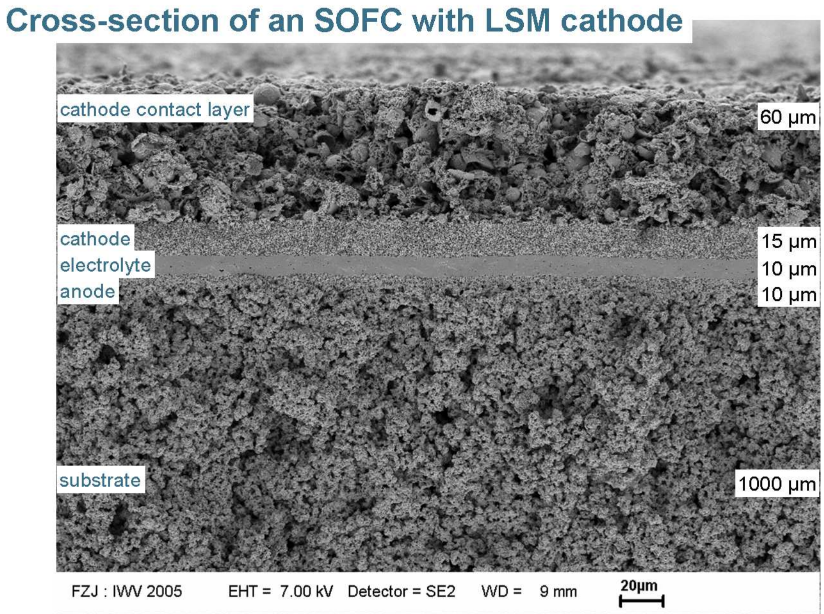

Figure 1.4: Cross-sectional view of the SOFC microstructure. The electrolyte and anode active layer are applied by vacuum slurry coating and the cathode active layer and cathode support layer are applied by wet powder spraying. Photo courtesy of Forschungszentrum Julich.

as a cathode; however, due to its high cost it was not feasible for use in commercial SOFCs. Perovskites were later used because of their comparatively low cost as well as possessing the required properties of an SOFC electrode. Lanthanum manganite based perovskites are currently the most common cathode material in SOFC electrodes. Although degradation of lanthanum manganites is not as severe as with other perovskites, such as LaCoO3, reactions with YSZ have been noted at high fabrication temperatures. $La_{0.8}Sr_{0.2}MnO_3$ (LSM) provides a good combination of electronic conductivity, expansion coefficient matching with YSZ, and is cost efficient.

Anode

Similarly to the cathode, the anode must also provide high electrical conductivity, high catalytic activity for the fuel oxidation reaction, and similar thermal expansion properties to other fuel cell components. In the first SOFCs, tested anode materials included platinum, gold, iron, and nickel. However, platinum does not last long in an operating fuel cell and, along with gold, is expensive. Nickel, on the other hand, performs well but is susceptible to aggregation at high temperatures, which inhibits fuel access. This problem can be solved by mixing yttria-stabilised zirconia (YSZ) particles with the nickel to form a composite electrode. YSZ provides an additional advantage as it creates an ion conducting phase within the electrode itself. The procedure of using composite materials has been adopted for both anodes and cathodes - Ni-YSZ for the anode and LSM-YSZ for the cathode. Composite electrodes have the advantage of providing far more triple phase boundary reaction sites than a single solid phase electrode.

Diffusion in Electrodes

The bulk diffusion of a species of gas depends on the properties of the gas itself, the properties of the species through which it diffuses, and the ambient conditions. In a porous structure, the pore walls block the movement of molecules and bulk diffusion no longer applies. Instead, an effective diffusivity, D_{eff}, is used to correctly represent the flux of molecules through a porous structure. The effective diffusivity is a function of the geometry of the porous media. Bruggeman [5] analyzed various physical characteristics of heterogeneous substances such as dielectric constants and conductivities. Bruggeman used many types of heterogeneous models including lamellae, imbedded spheres, and imbedded grains. For the imbedded spheres model, conductivity in both phases (sphere phase and bed phase) was derived analytically. If this model is used to describe porous media, with the sphere phase representing solid and the bed phase representing pore space, then diffusivity takes the place of conductivity. Bruggeman's derivation of conductivity (or diffusivity if phase is gaseous) is commonly called Bruggeman's equation:

$$D_{eff} = \varepsilon^{1.5} D_{bulk} \tag{1.16}$$

Where ε is the porosity of the structure (electrode in the case of fuel cells), and D_{bulk} is the diffusivity in open space of the diffusing gas. Porosity represents the ratio of pore space volume to total volume, and SOFCs typically have porosities ranging from 0.2 to 0.5. Tortuosity is a characteristic that describes how convoluted or meandering the flow paths are within a porous structure. Tortuosity is defined as the ratio of the average pore length, L_e, to the length of the porous medium, L, along the major diffusion axis.[6] The Bruggeman equation can be modified to reflect the effect of tortuosity on the effective diffusivity:

$$D_{eff} = \frac{\varepsilon}{\tau} D_{bulk} \tag{1.17}$$

Where

$$\tau = \frac{L_e}{L} \tag{1.18}$$

It is clear from this equation that the effective diffusivity of a given gas is greatly dependent on the porosity and tortuosity of the porous structure that it flows through.

However, there is a third physical characteristic of the solid structure that will also change the effective diffusivity: pore size. The Knudsen number, Kn, is a non-dimensional value that describes the ratio of wall collisions by molecules to the number of collisions molecules have with each other. Another way to represent this is by the following equation:

$$Kn = \frac{\langle\lambda\rangle}{d} \tag{1.19}$$

Where $\langle\lambda\rangle$ is the mean free path of the gas in question, and d is the mean pore size or characteristic length of the pore domain. The consequence of a large number of wall collisions on the effective diffusivity is known as the Knudsen effect, and when Kn becomes large (> 10) transport is described as Knudsen diffusion. Two additional transport regimes can also be described: bulk diffusion when $Kn < 0.01$, and the transition diffusion regime for $0.01 < Kn < 10$ [1]. The precise effect that the Knudsen number has on gas diffusivity is evident in the Bosanquet correlation:

$$D_{eff}^{Kn} = \frac{D_{eff}^{0}}{1 + Kn} \tag{1.20}$$

Where D_{eff}^{Kn} is the effective diffusivity with Knudsen effects taken into account, and D_{eff}^{0} is the effective diffusivity in the bulk diffusion regime ($Kn \to 0$). Combining equations 1.20 and 1.17 allows the determination of effective diffusivity using various porosities, tortuosities, and mean pore sizes.

1.2.5 CFD Modeling

Due to the complexities of the SOFC system, computational fluid dynamics (CFD) is an important method for testing various fuel cell properties in a time and cost effective manner. Geometries within a fuel cell such as the flow channel structure or the porous electrode are quite complex and can be difficult, if not impossible, to analyze analytically. Provided that an accurate mesh of control volumes (cells) can be constructed, CFD can be used to analyze very complex geometries.

Finite volume methods (FVM) are often employed in fuel cell computational models as well as in many fluid dynamics applications. The basic idea behind FVM is to split a 3D domain into many small control volumes, with a greater number of volumes providing greater accuracy. Transport equations are applied to each cell separately, however inputs and outputs at each cell face must match up with its neighbouring cells. At the boundaries of the domains, conditions must be known or assumed to give the data a point of reference. Within a fuel cell, mass transport within a flow channel is dominated by convection and therefore conservation of mass and momentum are the primary mass transport equations. Within a porous electrode, mass transport is dominated by diffusion and so the diffusion equation (detailed in chapter 3) is implemented. Heat transfer is also important within SOFCs, however this thesis only deals with mass transfer within electrodes.

1.3 Scope

The primary goal of this research is to develop a better computational electrode model using random packed spheres. Rather than continuing to use an overly simple domain of spherical particles that are supposed to represent non-spherical amorphous particles, this work will add features that help to construct a more realistic fuel cell electrode. The model is intended to be broad and encompass a variety of electrode materials and fabrication techniques. A literature review is performed to discover existing work done on the characterization of SOFC electrodes as well as computational micro-modeling techniques, including other randomly packed spheres models.

Two features were developed to improve the basic randomly packed spheres model: the ability to drop pore former particles along with ion and electrode conducting particles, and the ability to drop pre-agglomerated particles. For both of these features, their effects on diffusivity will be the primary characteristic investigated. This will be done by examining the three main geometrical properties that influence effective diffusivity: porosity, tortuosity, and pore size distribution. A relationship between diffusivity and both pore former volume fraction and pore former particle size will be determined. Also, it is to be determined if effective diffusivity changes when using pre-agglomerated particles for one or both phases.

A secondary goal of this research is to analyze various methods for measuring the pore size distribution in a porous electrode, and to propose a novel method that would enable the determination of local pore size within an electrode. Existing experimental and computational techniques are reviewed and a random walk method for determining pore size is chosen for pore size measurements in this thesis. This chosen method is also compared to the proposed novel technique to discover the validity of local pore measurements.

1.4 Organization of Thesis

Following this introduction, Chapter 2 proceeds to review recent literature that involves the micro-modeling approaches of SOFC electrodes. Chapter 3 will then explain how the Monte Carlo and CFD models presented in this paper were developed and applied. Chapter 4 will review the various techniques used to determine pore size distribution and mean pore size in a porous material. Also explored is the concept of determining a local pore size within a porous material and its potential applications. In Chapter 5, the results of the simulations are presented, as well as an analysis of the effects of recent changes to the model. Finally, Chapter 6 gives a summary of the work presented in this paper and includes suggestions about future work that may be done.

Chapter 2

Literature Review

2.1 SOFC Electrodes

2.1.1 Electrode Fabrication

SOFC electrodes are fabricated in many different ways, some of the more popular methods include: tape casting, screen printing, impregnation, and spraying methods. The method of fabrication will have a significant impact on the nature of the microstructural geometry. Tape casting [7, 8] involves the forming of a slurry into a thin tape ($10\mu m \sim 1000\mu m$). The tape can be joined to the electrolyte by hot press lamination and sintering. Screen printing [9, 10] involves the mixing of the electrode material (typically in a powdered form) with a binder and solvent to prepare an ink. The ink is applied through a woven mesh (or screen) and onto the electrolyte. Impregnation techniques [11] only work for composite electrodes. The YSZ phase is fabricated using one of the other techniques mentioned here (or any other for that matter). The electron conducting phase is then added to the porous YSZ by wet impregnation and then oxidized or reduced. This allows each phase to be added and hardened at separate temperatures.

Spraying methods [12, 13, 14] involve the spraying of the electrode material (typically as a slurry) directly onto the electrolyte or substrate. These techniques are of particular interest to this research because the dropping of particles, used in the computational creation of an electrode model in this thesis, mimics the action of spraying. Plasma spraying [13] is a specific spraying technique that utilizes plasma created by high-voltage electrodes to melt particles that pass through the plasma jet and deposit them on a substrate. If the particles are still liquid by the time they reach the surface, they flatten to form a splat.

2.1.2 Electrode Characterization

Recent research on SOFC electrodes have analyzed both anodes and cathodes in 2 dimensions [15, 16] as well as 3 dimensions [17, 18]. Other research collects electrode information in multiple 2D planes and interpolates that information to a 3D domain [19, 20, 21, 22, 23, 24]. The goal of many of these papers is to determine microstructural properties of typical SOFC electrodes in order to run electrochemical and mass transfer simulations with accurate geometric inputs.

Focused ion beam - scanning electron microscopy (FIB-SEM) technology has become a popular method for analyzing SOFC electrodes in 3D. This technology uses an SEM to photograph a 2D section of the surface of a porous electrode; the information is recorded as a 2D plane. A focused ion beam then shaves off a small amount from that surface and the SEM process is repeated. The end result is a series of 2D planes spaced apart by a small amount (resolutions of approximately 50 nm are possible) that can be interpolated and presented as 3D structures. Like most image processing procedures, the accuracy of this technique is dependant on its resolution.

Even resolutions as good as 50 nm will not exactly recreate an actual electrode since many particles and pores within the electrode are smaller than this. Figure 2.1 shows one such image of a 3D structure constructed using this FIB-SEM [20].

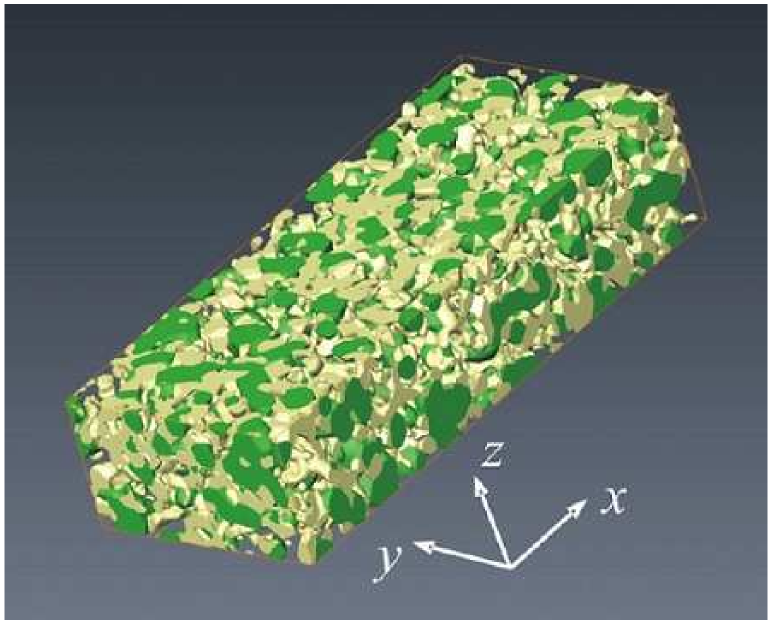

Figure 2.1: 3D image of an SOFC electrode reconstructed using FIB-SEM technology. Photo produced by Iwai et al.[20]

Wilson et al. [22, 23, 24] use FIB-SEM technology to reconstruct a sample SOFC electrode. The Triple phase boundary (TPB) density, phase connectivity and phase tortuosity of an LSM-YSZ cathode are measured using this 3D analysis method. Also, the FIB-SEM technology is used to explore the relationship between composition and performance in a Ni-YSZ anode. Iwai et al. [20] also use an FIB-SEM system to evaluate microstructural characteristics of a Ni-YSZ anode. TPB density is quantified here by two methods: a volume expansion method and a centroid method. Tortuosity is also evaluated by two methods: a random walk calculation and a lattice Boltzmann method based calculation. For both the TPB density and tortuosity, the compared methods yield similar results. Shearing et al. [21] also use FIB-SEM to reconstruct the microstructure of an SOFC anode. The electrochemical performance ascertained from the model is compared to the electrochemical performance characterized by electrochemical impedance spectroscopy (EIS). The reconstructed model provided consistent results in comparison to EIS. Gostovic et al. [19] use the FIB-SEM technique in similar fashion to observe how microstructural characteristics such as porosity, average pore diameter, tortuosity and TPB length of a cathode change as sintering temperature changes. Performance characteristics are also correlated to microstructural properties determined from the FIB-SEM reconstructed electrode.

Lanzini et al. [15] obtain electrode statistics from 2D SEM and TEM images. Various microstructural characteristics are analyzed including phases' fraction, grain size and shape, and phase spatial organization. Using these characteristics, a random, porous 3D structure is constructed in a discrete grid. Shikazono et al. [16] look at microstructure and polarization characteristics of an SOFC anode for co-precipitated and mechanically mixed anode fabrication processes. Low voltage SEM-EDX is used to characterize the microstructure of both fabrication processes using various amounts of acrylic pore former. Relationships between polarization resistance and various microstructural characteristics such as circularity, three-phase boundary length, and contiguity are investigated.

Izzo et al. [18] use X-ray computed tomography (XCT) to visualize a 3D image of an SOFC electrode at resolutions better than 50 nm. Microstructural characteristics are determined using a 3D model reconstructed from the XCT image. Porosity is calculated using a voxel counting method and tortuosity is evaluated by solving the Laplace equation. The microstructural characteristics taken from XCTs are used as inputs for simulations of mass transport and electrochemical reactions. Like FIB-SEM, XCT techniques are only as accurate as their resolution.

2.2 Micro-modeling

Much recent work on the micro-modeling of fuel cells involves creating computational domains which consist of randomly placed spheres to represent solid particles [25, 17, 26, 27]. While the goals of these works are typically similar, the way in which the domains are constructed are often different.

Grew et al. [17] implement a Monte Carlo, packed spheres model with the purpose of developing quantitative characterization and analysis tools that can be used on a 3-dimensional XCT reconstructed electrode. The building process in this work involves placing all YSZ particles across the 3D domain by randomly choosing x-, y-, z-coordinates to grow them from. This is followed by the random placement of all Ni particles across the domain allowing the YSZ phase to be overwritten. Golbert et al. [25] also detail a method for building a randomly packed spheres model. The algorithm involves choosing a random point within the domain to place a particle, additional particles are then grown adjacent to already placed particles until the domain is full. Pore former particles along with electron and ion conducting solid particles are used. After all particles are placed, each sphere is grown slightly to simulate the effect of sintering in the electrode. The purpose of the model is to determine percolation and triple phase boundary data for use in the calculation of transport and redox reaction simulations. Jeon et al. [26, 28] use a simple cubic lattice of spherical particles to represent the electrode. Each particle is randomly assigned to be either an ion conducting particle or an electron conducting particle.

Kenney et al. [27, 29] use a randomly packed spheres model as well. This particular algorithm drops spherical particles from the top of the domain until they touch an already placed particle, at which point they continue to roll until touching at least three other particles. This particular method formed the basis of the model used in this thesis and a more detailed description can be found in Chapter 3. Choi et al. [30] use the model proposed by Kenney et al. [27] to create three types of 3D computational grids: cartesian, octree, and body-fitted. An FVM is applied to the mesh to determine effective transport properties in each phase (pore space, electron conducting, and ion conducting). This is done for mono-sized distributions of particles as well as realistic poly-disperse distributions that were determined in other literature.

2.3 Pore Size Analysis

Chapter 4 explains how various pore size measurement techniques work. This section will detail other works that apply pore size measurement techniques and the purposes for which the techniques are used.

The morphological opening method is used in Schulz et al. [31] to determine pore size in a polymer electrolyte fuel cell electrode. The fibrous structure of the gas diffusion layer is reconstructed using a stochastic technique. Pore sizes are used to help solve for the capillary pressure-saturation relationship. Kim et al. [32] reconstruct the catalyst layer of a proton exchange membrane fuel cell. Geometric properties are then characterized, including pore size using the morphological opening method. Effective transport properties are calculated using a variety of techniques.

Berson et al. [1] use a random walk algorithm that traces chords from a single particle that bounces off solid particle walls within the pore space. This particular algorithm can also be used to measure self-diffusivity and has been implemented before in literature [33, 34]. Berson et al. demonstrate that this method can be used to determine a characteristic length of a porous structure to represent mean pore size. This characteristic length must be used in order to properly account for Knudsen effects in a porous structure. Figure 2.2 displays results acquired by Berson et al. that show how characteristic length is the proper length scale when calculating Knudsen number by comparing various pore size measurement techniques to the Bosanquet correlation (1.20). Berson et al. also determine that for porosities below approximately 0.4, the Bruggeman equation does not accurately describe diffusion in random packings of spheres. Instead an alternate equation is proposed:

$$\frac{D_{eff}}{D_{bulk}} = 1.6\varepsilon^2 \quad for\ \varepsilon \leq 0.4 \tag{2.1}$$

For $\varepsilon > 0.4$ the Bruggeman equation (1.16) was shown to fit effective diffusivity data accurately.

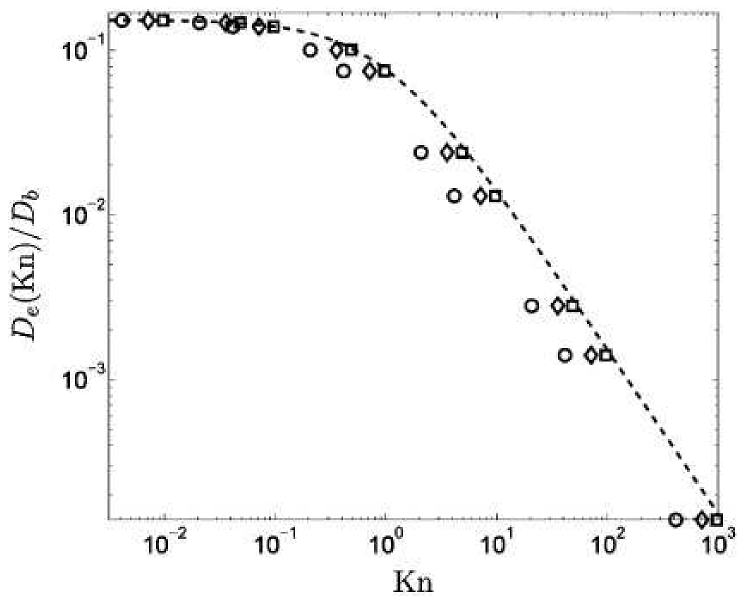

Figure 2.2: Various methods of characterizing pore size compared to the Bosanquet correlation. ○ is based on a mean pore size found with a morphological opening type algorithm. ◇ is based on the mean chord length $\langle l \rangle$ from the random walk algorithm. Square is based on the characteristic length d. Photo produced by Berson et al.[1]

Chapter 3

Modeling Techniques

3.1 Existing Model

The random sphere model presented in Kenney et al. [27] provides the framework for which the model presented in this thesis is based. The algorithm used to create the model was written in C programming language. A porous volume consisting of one or two solid phases is made up of randomly distributed spherical particles. This distribution is achieved by randomly dropping particles one at a time into a 3-dimensional domain. Typically, particle size distributions are of a normal Gaussian distribution, but any type of distribution is possible. Particles fall and are allowed to roll over each other until the falling particle is touching at least 3 other particles or is resting on the bottom of the domain. The x- and y- boundaries are periodic during the dropping phase; this means if a particle moves through an x- or y- boundary plane, it will appear at the other end of the domain. During the fabrication of a real SOFC, the electrode undergoes a sintering process. In this model, the particles are allowed to overlap each other slightly to simulate the effect of sintering. In Choi et al. [30], the minimum acceptable domain size for this model was determined to be

$10d_p \times 10d_p \times 10d_p$, where d_p is the solid particle diameter.

Various physical characteristics of the model can be specified before the particles are distributed. The adjustable parameters are porosity, volume fraction of each solid phase, mean diameter of solid particles, standard deviation of particle diameters, neck growth (if any), and size of domain. The porosity is achieved iteratively by altering the overlap - porosity increases as overlap decreases, and decreases as overlap increases. However, achieving desired porosity in this manner has drawbacks. For one, there will be a maximum porosity when the particle overlap approaches zero. In the case of this model, the maximum porosity is approximately 44%. The second drawback is that when the overlap is very small, the realism of the model decreases because a random sphere model with a high overlap is believed to better represent the geometry of a real SOFC electrode (Figure 2.1). Amorphous particles can be represented by groups of spheres only if the overlap is sufficiently large.

Other physical characteristics of the model can also be determined after particle placement. Programs also written in C programming language allow the determination of pore size distribution, triple phase boundary length, solid phase surface area, contact area, and percolation of each phase. After particle placement, the centre coordinates, the particle diameter, and the index values of all contacting particles are known. Knowing which particles are contacting allows the determination of those particles that are part of a percolating network.

The pore size distribution is solved using a sphere growth - chord length hybrid method described in Section 4.1.3. The grown spheres tend to underestimate the pore size while the chord length method proved more accurate. The triple phase boundary length, solid phase surface area, and solid phase contact area are solved simply by knowing the centre coordinate and size of each particle. Figure 3.1 illustrates how triple phase boundary length and solid phase contact area can both be solved analytically for two contacting particles. Adjustments were then made for cases of multiple contacting particles.

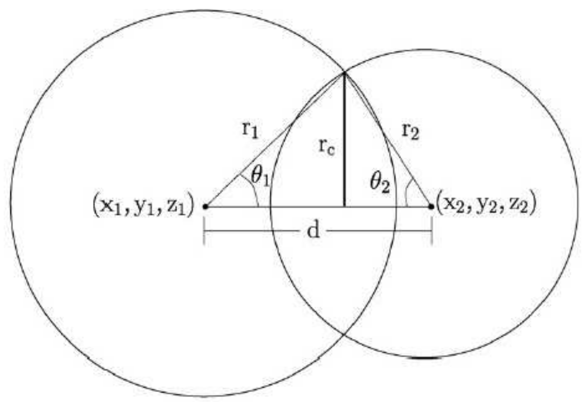

Figure 3.1: Geometrical relationship of two overlapping spheres [27]

3.2 Improvements to Existing Model

The bulk of the work presented in this thesis involved altering the existing model from above to better represent a real electrode. The need for this arose from comparison of various random sphere models (including the model above) with recent images obtained from FIB-SEM technology. It can be seen from Figure 2.1 that the solid particles of an SOFC electrode are more like amorphous shapes rather than spheres. However, groups of spheres can be agglomerated together to better represent amorphous shaped particles.

Also, as mentioned in section 3.1, the porosity of the model is altered by changing the amount of overlap (or sintering) when the particles are placed; using this method creates serious limitations. The ability to add pore former particles to the model was implemented to correct these limitations, which in turn led to the ability to create more realistic electrodes with a larger range of porosities.

3.2.1 Addition of Pore Former

In order to include pore former in the random sphere model, the particle dropping algorithm had to be changed so that a third solid phase (pore former) was dropped along with the other solid phases (electron and ion carrying phases). In the C program that places the particles, the pore former solid volume fraction is now specified along with the other two solid phases. The average particle size and the standard deviation of the particle size distribution are also specified for the pore former phase. Pore former particles are then dropped along with the other two solid phases and are allowed to settle in the same fashion. After all three phases of particles have filled up the domain, the centres and radii of the electron and ion transporting particles are stored as usual. However, the centres and radii of the pore former particles are not recorded, effectively removing them from the domain and leaving pore space in their locations.

3.2.2 Agglomerated Particles

The geometry of an actual SOFC electrode is made up of amorphous and irregular shapes of solid particles. For a random sphere model to capture this geometry, irregular solid shapes can be made from agglomerates of multiple solid spheres. With a high enough overlap, dropping one sphere at a time may allow particles to agglomerate naturally at some locations, but this is random and unreliable. In a real electrode, the solid particles will agglomerate when mixed in an ink or slurry. Further agglomeration may occur when the electrode is heated, i.e. during manufacturing or sintering. Simulating this effect in a model after the particles have been dropped is very difficult. A simpler solution would be dropping already formed agglomerates instead of single particles.

In the model presented in this paper, four spherical particles are agglomerated in a square shape as illustrated in Figure 3.2. This square shape is allowed to rotate along the z-direction randomly before dropping. It then falls like the old single particle dropping algorithm and comes to rest when it is touching enough already placed particles or when it reaches the bottom of the domain. As the agglomerate drops, the algorithm is constantly checking each of the four particles for contact with an already placed particle. When three of the four particles are touching, the agglomerate stops moving and is in its final resting place. When two of the four particles make contact, those particles stick while the rest of the agglomerate is allowed to rotate until a third agglomerate particle makes contact. When only one of the four particles makes contact, that particle then translates vertically upward and horizontally. The other three agglomerate particles also translate horizontally but continue moving in the downward vertical direction. This particle movement simulates a bouncing and rotating motion when only the corner of the agglomerate makes contact. One or both solid phases can be dropped as agglomerates. This paper only explores square shaped agglomerates of 4 spheres; however, the C program that was written can quite easily be altered to drop any shaped agglomerate.

When single spheres are dropped they naturally pack quite easily because of their shape. However, when agglomerates are dropped, they do not necessarily pack nicely

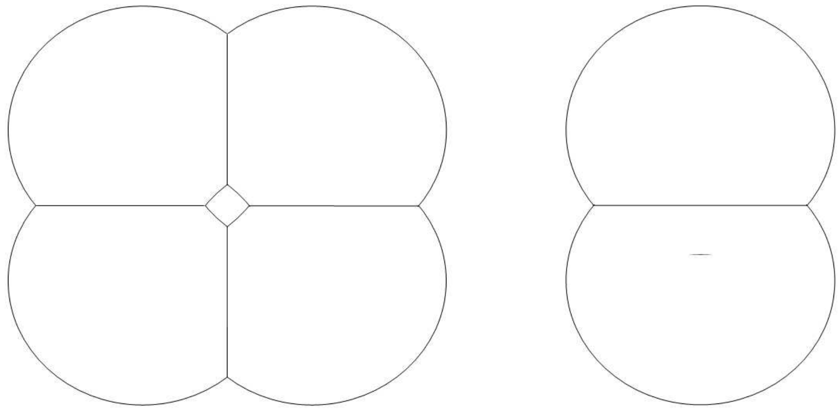

Figure 3.2: Drawing of the four particle agglomerate from the top and side.

due to their irregular shape. This means that in order for the agglomerate algorithm to achieve the same porosity as the single sphere algorithm, the overlap must be greater. Therefore, the lower limit of porosity is much higher for the agglomerate algorithm than for the single sphere algorithm. A positive effect though, is that low overlaps are generally unrealistic in comparison to actual electrodes; so the high overlap of the agglomerate algorithm is beneficial in this respect.

3.3 Solving Diffusivity

After the particles have been placed and the geometry is set, simulations can be run and diffusivity solved. Two methods for computationally solving for diffusivity are presented in this section: a random walk simulation and a finite volume method (FVM) simulation.

3.3.1 Random Walk Simulations

Random walk algorithms encompass all mathematical models that consist of a path which takes successive random steps around a domain. Random walk algorithms are not only used for describing diffusion but are also applicable to economics, computer science, and psychology to name a few. Brownian motion is a random walk model used to describe the path of a particle suspended in a fluid.

The method employed for determining diffusivity takes single particles, one at a time, and lets them take a random walk through the pore space of the electrode structure. This method has been used before in Berson et al. [1] and relies on the basic principles of Brownian motion. In this work, Brownian motion describes the self-diffusion of a gas due to the irregular movement of gas molecules. Equation 3.1 represents the relationship of the self-diffusion coefficient (D) of a gas to the mean square displacement ($\langle \xi^2 \rangle$) of a large number of gas molecules [1].

$$D = \frac{\langle \xi^2 \rangle}{6t} \tag{3.1}$$

The algorithm begins by randomly positioning a particle within the pore domain and allowing it to randomly travel in a straight line until it contacts another gas particle, or the surface of the solid phase. As only one particle takes a random walk at a time, there are no actual gas particles to come in contact with. Instead, a free path, λ, is taken from an exponential probability distribution centred on the mean free path of the gas. The particle travels this distance in a straight line, then a new random direction is chosen along with a new free path, and the particle continues on. The particle is allowed to bounce around the pore space until it has traveled a prescribed distance, s. Time, t, can be ascertained from the following equation:

$$t = \frac{s}{v_T} \tag{3.2}$$

where v_T is the thermal velocity of the gas particle in question. After the particle is finished traveling, the displacement, ξ, between the initial position and the final position of the particle is measured. This process is repeated for many more particles and the self-diffusion coefficient can be calculated from equation 3.1. The self-diffusion coefficient is multiplied by the porosity to obtain the effective diffusivity, D_{eff}.

When a particle contacts the solid phase before it has traveled its free path, it must reflect back into pore space. This random walk method assumes that the particle is reflected according to the law of diffuse reflection; i.e. the angle of redirection follows Knudsen's cosine law. The angle of redirection is taken from an angular probability distribution which is defined with respect to the normal angle to the solid surface. The boundaries of the domain during this algorithm are assumed to be symmetrical.

As Berson et al. [1] suggests, the distance each particle travels is $s = 500L$, where L is the side length of the domain. Also, the number of particles used for each test is at least 2000 as was used in Berson et al. For each set of physical properties in this study, diffusivity is determined for four random structures.

3.3.2 Finite Volume Method Simulations

The structures created in this study are all analytical geometries (i.e. domains consisting of sphere centre coordinates and sphere radii). However, it is helpful to be able to solve discrete geometries made up of many control volumes as computational domains are often presented in this fashion. To solve the diffusivity of a discrete geometry, FVM can be applied, and for this a CFD code must be used. Also, FVM solutions allow for easy visualization with tools such as Tecplot and Paraview whereas random walk solutions do not afford this. OpenFOAM [35] was the CFD tool used for all FVM simulations in this study.

Meshing

After all solid particles are placed, the information of the final structure is stored as sphere centre coordinates and sphere radii. This information is imported into OpenFOAM so that the location of each of the three phases (2 solid and 1 pore) is known during the meshing process. The simplest mesh would be to overlay a cartesian grid across the entire domain. However, in order to provide adequate accuracy, a cartesian grid must be so fine that the required computing power becomes unmanageable. OpenFOAM provides a tool known as *snappyHexMesh* that solves this issue. This utility allows a body fitted grid to be implemented so that large cells are present deep within each phase, while small cells are present at and near the phase boundaries.

A *snappyHexMesh* grid must always begin with a cartesian grid base. In this study the base grid is made of 6.4×10^4 cubic control volumes (40 x 40 x 40). The *snappyHexMesh* is then implemented; it begins by determining which cells contain phase-to-phase interfaces. Each of these cells are then split into 8 smaller cubic cells, each with a side length half that of the original cell. This process continues to split cells that contain phase-to-phase interfaces until a desired refinement level is reached or a desired number of total cells. At this point, the small cells that still contain phase interfaces are 'snapped' so that the phase interface makes up one of the faces of the cell. These cells will differ from all others in the fact that they are no longer cubic. Figure 3.3 illustrates the various steps of *snappyHexMesh* [35].

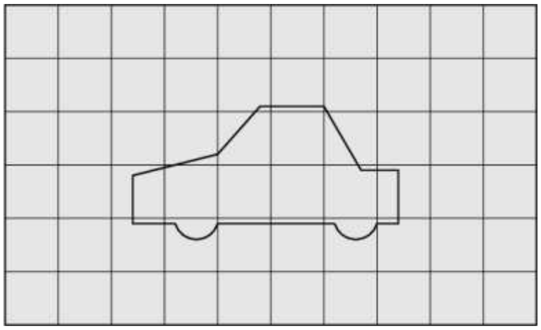

(a) Cartesian base mesh

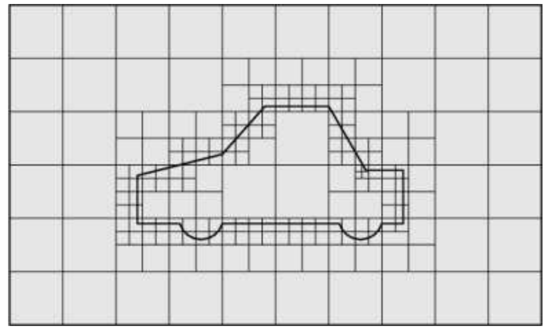

(b) Splitting cells containing phase boundary

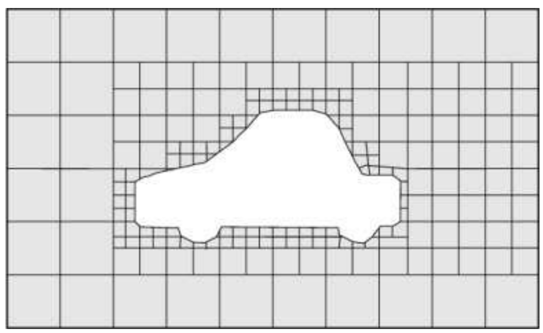

(c) Final 'snapped' mesh

Figure 3.3: Steps to create a snappyHexMesh. [35] on a 2D domain.

At this point, the mesh has identified the phase boundaries, however it has not identified which phase is which. An OpenFOAM utility called *setSet* is used to identify each phase. It checks each particle (using centre coordinates and radii) and determines which cells are contained within the sphere and assigns that particular cell to be part of the correct phase. All cells not contained within a sphere are assigned to the pore phase. Because of particle overlap, there will be certain cells that are assigned to both the electron conducting and ion conducting phases. For each overlap, the cells contained within are randomly deleted from a phase so that each cell in the domain is part of only one phase.

The final step is to use another OpenFOAM utility known as *splitMeshRegions*. This tool finds regions within the domain that are isolated from the rest of its phase. For each phase, this allows the separation of cells that are part of the main percolating network from the cells that are isolated and not part of any percolating network. The *setSet* command is used once more to define six separate 'children' meshes that fit together to form one complete 'parent' mesh: electron, ion, pore, nelectron, nion, and npore. Each parent mesh in this study contains approximately 3×10^6 cells.

Solving

The diffusivity equation (3.3) is the general equation used for FVM since the transport of gas is assumed to be dominated by diffusion. D_{bulk} represents the diffusivity in open space of the diffusing gas, and ϕ is the concentration/density of the diffusing gas at a given location. Dirichlet boundary conditions are imposed at the top and bottom of the domain, i.e. $\phi = \phi_1$ and $\phi = \phi_0$, and symmetry boundary conditions are imposed on the remaining four sides.

$$\nabla \cdot (D_{bulk} \nabla \phi) = 0 \tag{3.3}$$

This general equation is then transformed into a discretized form so that it may be applied to an FVM. For more information regarding the FVM solution applied in this research, the reader is referred to Choi et al.[30]

Chapter 4

Pore Size Measurement and Analysis

4.1 Pore Size Measurement Methods

Characterization of pore size within a porous structure is a complex exercise. There is an ambiguity of what exactly constitutes a pore and in what direction its diameter should be measured. The simplest geometry for the measurement of pore size is a porous structure with a series of straight parallel channels; pore size is simply the diameter of the channel. This geometry does not represent a realistic SOFC electrode. Instead, the pores of an SOFC electrode are far more tortuous and have unpredictable, irregular shapes. This section consists of various methods of characterizing the pore size distribution of a porous electrode. Section 4.1.1 explains a typical method for experimentally determining mean pore size, while Sections 4.1.2 and 4.1.3 cover computational methods for calculating pore size.

4.1.1 Mercury Intrusion Porosimetry

Mercury Intrusion Porosimetry (MIP) is an experimental technique often used to determine mean pore size and other pore-related properties within a porous structure.

"Porosimetry" refers to the measurement of pore size, pore volume, pore density, and other characteristics involving porosity. Mercury is a liquid that does not wet most solids and does not spontaneously penetrate pores. An external pressure is required to force mercury to infiltrate the pores of a porous structure. The required pressure is inversely proportional to the size of the pores, only slight pressure is required to intrude mercury into large pores while intrusion into small pores requires a large pressure. In practice, mercury is gradually intruded into a porous structure under an increasing controlled pressure. From pressure versus intrusion data, pore volume and size distributions are determined [36]. However, a major drawback of this technique is that it assumes the pores can be represented by a bundle of tubes; this assumption is often invalid for porous media such as SOFC electrodes.

4.1.2 Sphere Growth Methods

Two different sphere growth methods will be presented; both involve picking a point within the pore space and growing a sphere until a set of conditions are met. The first method involves randomly picking a point within the pore space and setting that point as the centre of the soon to be grown sphere. The sphere then grows from that point until its surface makes contact with the solid phase of the porous structure. The sphere then stops growing and a new random point is chosen and the process repeats. After a reasonable number of spheres are collected, their diameters can be analyzed as the pore size distribution for the domain. Unfortunately, this method generally underestimates the pore size distribution since the spheres rarely fill the entire pore they grow in.

The second method is known as the morphological opening method. This method starts similarly to the last method with a random point being chosen within the pore space. A sphere is grown from this point, however the centre of the sphere is not fixed. Instead, as the surface of the sphere comes into contact with the solid phase, the centre of the sphere is allowed to translate in any direction to allow room for the sphere to continue growing. This allows for the sphere to fill up the entire pore until it cannot grow anymore even by translating. Like the last method, after a number of spheres have been grown, their diameters can be collected to represent the pore size distribution.

4.1.3 Chord Length Methods

There are a few similar but slightly different pore size measurement techniques that involve the collection of chord lines to represent pore diameters. The most basic of these techniques works in a similar way to the first sphere growth method above. A random point is chosen within the pore domain and a chord is drawn in a random direction from that point until it contacts the surface of the solid phase. The chord is then extended in the opposite direction from the random point until it too comes into contact with the solid phase. The total length of the chord - from one solid surface to the other - is recorded as the pore size. The process is repeated with a new random point until a large enough distribution of chords has been collected. A drawback of this method is that, because of the randomness of the chosen direction, chords will often measure the length of the pore rather than the width; resulting in an over estimate of pore diameter. The extreme of this situation may occur in the unlikely case where a diffusion path exists with a tortuosity very close to 1. In this case it is conceivable that the chord may pass straight through the domain without ever coming into contact with a solid surface and appear to be infinite in length.

Another computational technique is actually a hybrid method that combines the sphere growth method with the chord length method and was analyzed in Kenney et al.[27] Similarly to previous methods, a random point is chosen within the pore space. A sphere with a centre fixed at that point is grown until its surface makes contact with the solid phase. At this point, a chord is drawn from where the sphere makes contact with the solid phase, through the centre of the sphere, and continues to extend until it makes contact with another part of the solid phase. A large collection of these chords are analyzed as the pore size distribution. This technique can be preferable to the first method of this section since the direction of the chord is more likely to extend across the pore width and not the pore length.

Method Used For Current Study

The final computational technique described is the one that is used for pore size analysis in this thesis (within Chapter 5) and was presented in Berson et el.[1] This technique was ultimately chosen because Berson et al. [1] show that the length scales provided by this method allow accurate calculation of Knudsen diffusivity (Figure 2.2). To gather the necessary chords, an algorithm nearly identical to the random walk diffusivity solution (outlined in Section 3.3.1) is implemented. The only difference of this algorithm is the mean free path is set to an unrealistically large value so that only wall collisions are present within the simulation. The result is a single particle which traces out a series of chords that are connected end-to-end. In this study, 1000 particles were bounced around the pore space creating approximately 1000 chords each, resulting in a total of approximately 1×10^6 chords per structure. This collection of chords is used to represent the pore size distribution.

Berson et al. [1] also illustrated a way to represent mean pore size that better agrees with Knudsen effects than any method outlined above: using the collected chords to determine a characteristic length. This method has also been used before by Levitz and Zalc et al. [33, 34]. The distribution of chords is used in equation 4.1 to determine a characteristic length, d, where $\langle l \rangle$ is the distribution of chords, and β depends on the model for wall collisions.

$$d = \left(\frac{\langle l^2 \rangle}{2\langle l \rangle^2} - \beta \right) \langle l \rangle \tag{4.1}$$

with

$$\beta = -\sum_{j=2}^{\infty} \langle \cos \gamma_{1j} \rangle \tag{4.2}$$

γ_{1j} is the angle between the first chord and the jth chord. The first term within the brackets of equation 4.1 depends on the first two moments of the chord length distribution and should equal 1 for an exponential chord distribution. The second term, β, should be equal to 0 for specular reflections, but for diffuse reflections $\beta \approx 4/13$, which was verified by Zalc et al.[34] With this characteristic length representing the mean pore size, Knudsen effects can be accurately considered, as evidenced in Figure 2.2 from Berson et al.[1]

4.2 Local Knudsen Effects

When solving diffusivity using FVM techniques, each cell is solved separately without Knudsen effects taken into account. When a final diffusivity is attained, equation 1.20

is applied to the entire domain for a known mean pore size (characteristic length). But what if Knudsen effects were considered at the cell level? CFD results show that certain diffusion paths within a domain are favored over others. If Knudsen effects were considered locally then perhaps some of these favored diffusion paths would actually prove too small for gases to travel through effectively. Perhaps a highly tortuous, large diameter diffusion path would instead be favored. It is possible that solving diffusivity using FVM techniques could be improved if local Knudsen effects are considered.

4.2.1 Measuring Local Pore Size

The first step in applying local Knudsen effects is to accurately measure local pore size across the entire pore domain. To do this, a random walk algorithm is not suitable because there is no guarantee that the entire pore space will be measured. For a local Knudsen number to be applied in an FVM solution, the local pore size must be known throughout the entire pore domain. To accomplish this, a structured pore measuring technique must be implemented that retains the accuracy of the random walk method detailed in Section 4.1.3.

The proposed algorithm begins by populating the whole domain (solid and pore space) with evenly spaced starting points. A cubic domain will have $p \times p \times p$ starting points, each the same distance away from its nearest neighbours. The starting points that are within the solid domain are then eliminated. From each of the remaining starting points a large number of chords are extended in random directions until both ends of the chord come into contact with a solid particle. The total length of all chords at each starting point is at least 500 times the size of the domain side length for the study presented here. In the future, a study must be done to determine the sufficient number of chords at each starting point. The number of starting points used will vary depending on the computational size of the domain. This technique does not allow for the β value to be calculated because it is not a true random walk algorithm. Instead, β will be estimated to be 4/13 at all times since this is the expected value for diffuse reflections [1, 34]. Characteristic length can then be determined for each starting point and a local Knudsen number is determined.

4.2.2 Comparison to Random Walk Method

To determine the accuracy of this method, its results will be compared to the random walk method used for the rest of this study (i.e. Chapter 5 results). The structures used in this section are the same domains used for the pore former volume fraction study (section 5.1.1) in the next chapter. Instead of determining local characteristic length, all chords from every starting point are used together to determine an overall characteristic length. Although this isn't the intended method of analysis for this technique, it is the only way to directly compare structured pore size measurements to the random walk method.

Figure 4.1 displays the relationship between mean pore size and pore former volume fraction. All characteristics of the physical domain are the same as in section 5.1.1 in the next chapter; the only difference being the pore size measurement technique. As it turns out, the measurement techniques are not totally in agreement. Referring to Figure 5.3 in Chapter 5, the mean chord length for both cases ranges between 0.035 and 0.065, and the characteristic length ranges between 0.025 and 0.050. In Figure 4.1 the mean chord length for the two cases ranges between 0.055

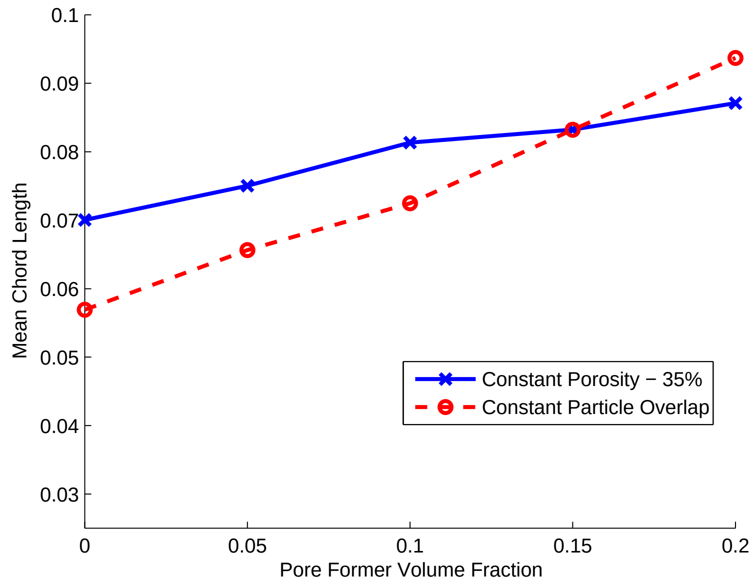

(a) Mean Chord Length

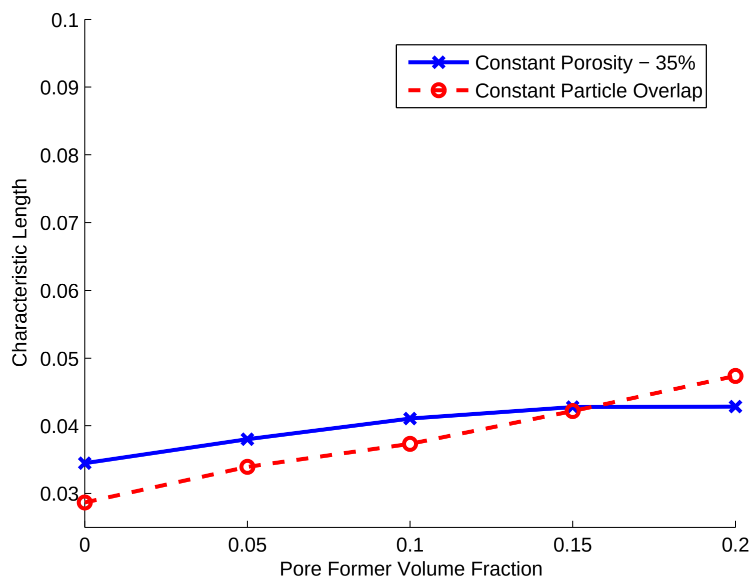

(b) Characteristic Length

Figure 4.1: Relationship between mean pore size (represented by both chord length and characteristic length) and volume fraction of pore former using a structured measurement. Pore former particle size to solid particle size ratio is 1:1. All results are in ratio to a domain side length of 1.

and 0.095, and the characteristic length ranges between 0.025 and 0.050. The general slope of the lines are very similar for both pore size measurement techniques, however the structured measurement technique overestimates the mean chord length by 45% to 55%. Even with this large error in mean chord length, the error in characteristic length is less than 5%.

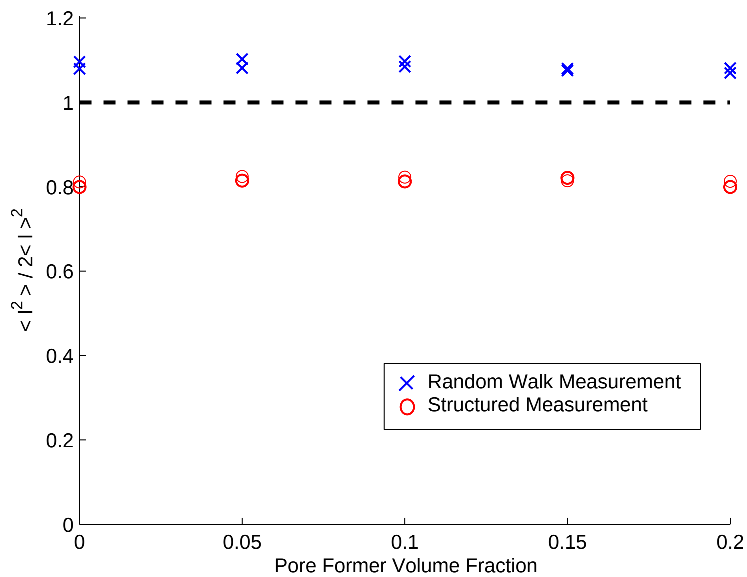

Figure 4.2: $\langle l^2 \rangle / 2 \langle l \rangle^2$ as a function of pore former volume fraction. The dashed line represents the expected value of 1 for an exponential distribution of chords.

Figure 4.2 provides explanation as to why the error in mean chord length is so large while the error in characteristic length is so small. The ratio $\langle l^2 \rangle / 2 \langle l \rangle^2$ is equal to 1 for exponential chord length distributions. The random walk algorithm calculates this ratio to reside in the range of 1.05 to 1.1; very close to an exponential distribution. The structured pore measurement algorithm calculates a ratio of approximately 0.8, which is in total disagreement with the random walk algorithm. Referring to equation

4.1, there are 3 terms that affect characteristic length: the ratio $\langle l^2 \rangle / 2\langle l \rangle^2$, the mean chord length $\langle l \rangle$, and β. β is approximately 4/13 for both measurement techniques. The structured pore size measurement underestimates the ratio $\langle l^2 \rangle / 2\langle l \rangle^2$, while overestimating the mean chord length $\langle l \rangle$. The end result is that the errors in both these terms cancel out, and an accurate characteristic length is calculated. However, this is due to a large amount of luck and the structured method still needs alteration and improvement before it can be successfully implemented.

Chapter 5

Characterization of New Features

With the addition of pore former particles and agglomerates of the solid phases, the geometry of the model is certain to change. The determination of how the new features change the geometry, whether for better or worse, is of great importance. This study will be conducted using both random walk methods as well as finite volume methods. Results from the random walk methods are presented in this chapter. For finite volume calculations, visual results created with the program Paraview are presented in this chapter, while quantitative values of diffusivity are found in Appendix B.

5.1 Pore Former Particles

Dropping pore former particles creates pockets of pore space within the solid porous electrode. Testing the effect of pore former particles in this model is done in two major ways: observing the effects of various pore former volume fractions and observing the effects of various pore former particle sizes. Three major characteristics will be studied: pore size distribution, tortuosity, and effective diffusivity.

5.1.1 Effect of Altering Pore Former Volume Fraction

Five levels of pore former volume fraction were tested in simulations: 0%, 5%, 10%, 15%, and 20%. The pore former particles, ion conducting particles, and electron conducting particles are all the same size (mono-sized). The structures were generated using the random sphere dropping method with the ability to drop pore former particles included. As the amount of pore former is increased, either the porosity and/or the particle overlap length (i.e. amount of sintering) must increase to compensate. In this study, two situations will be analyzed: constant porosity as pore former is added, and constant particle overlap as pore former is added. A porosity of 35% is used for the case of constant porosity, while porosities ranging from 25% to 39% are used for the case of constant particle overlap.

While holding porosity constant as pore former is added, the particle overlap will increase. Physically, this represents an increase in the level of sintering with greater volumes of pore former. Figure 5.1 displays 3-dimensional structures of the random dropped spheres model with two different amounts of pore former. Close inspection of these views demonstrate that with the porosity held constant, the solid particle overlap increases to allow the pore former particles room to fit without increasing porosity.

The other situation analyzed involves holding the particle overlap constant, which results in an increase of porosity as more pore former is added. This situation is probably more practical than that of the increase in particle overlap since the purpose of pore former is typically to increase porosity. Figure 5.2 displays another pair of 3-dimensional structures created using the random dropped spheres model. In this case, the particle overlap is held constant and with more pore former particles, there

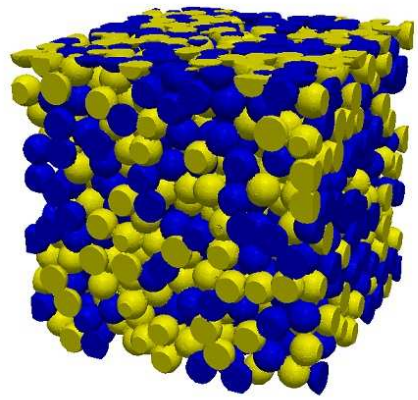

(a) Low particle overlap and 0% pore former volume fraction

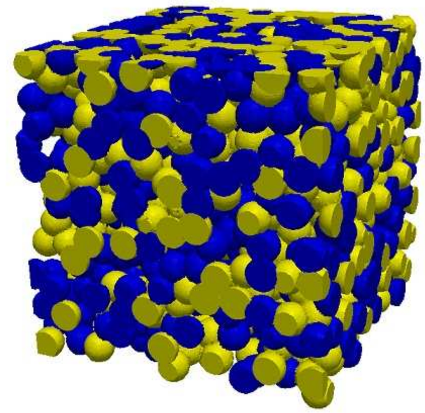

(b) High particle overlap and 20% pore former volume fraction

Figure 5.1: 3D model of a $10\mu m \times 10\mu m \times 10\mu m$ section of SOFC electrode with a constant porosity of 35%.

is a higher porosity and therefore fewer solid particles in a given volume.

Pore Size Distribution

Using the random walk method of collecting chord lengths in the pore space, the average pore size can be quantified and a relationship with pore former volume fraction is found. Altering the pore former volume fraction will also change the shape of the pore size distribution curve. Holding porosity constant as pore former volume fraction is increased yields different results than the case of constant particle overlap as pore former volume fraction is increased.

In Figure 5.3, both cases of constant porosity and constant particle overlap are plotted together for comparison. Each side length of the domain is a standard size of 1, while the particle size of all solid phases (ion and electron conducting, and pore

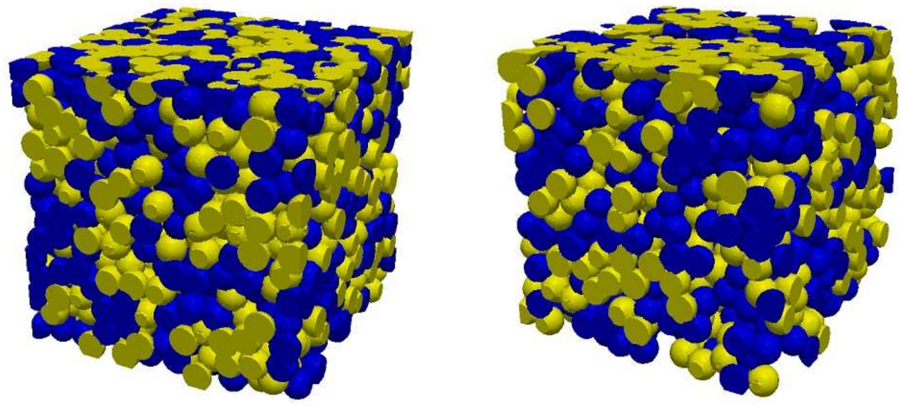

(a) 25% porosity and 0% pore former volume fraction

(b) 39% porosity and 20% pore former volume fraction

Figure 5.2: 3D model of a $10\mu m \times 10\mu m \times 10\mu m$ section of SOFC electrode with constant particle overlap.

former) is 0.1. In both cases, as pore former volume fraction is increased, the average pore size of the electrode increases at a near linear rate. When no pore former is used, the average pore size is 0.038 and 0.047 for porosities of 25% and 35% respectively. Since the pore former particle size is the same as the solid particle size, it makes sense that the average pore size will grow closer to 0.1 (same size as solid particles) as the pore former volume fraction increases.

The difference between the cases can be attributed to the effect of porosity on average pore size. In Berson et al. [1] it was shown that a relationship exists between porosity and average pore size where average pore size increases linearly as porosity increases. Therefore, in the case of constant porosity, only pore former volume fraction has an effect on the pore size. However, in the case of constant particle overlap, both the change in porosity and the change in pore former volume fraction have an effect

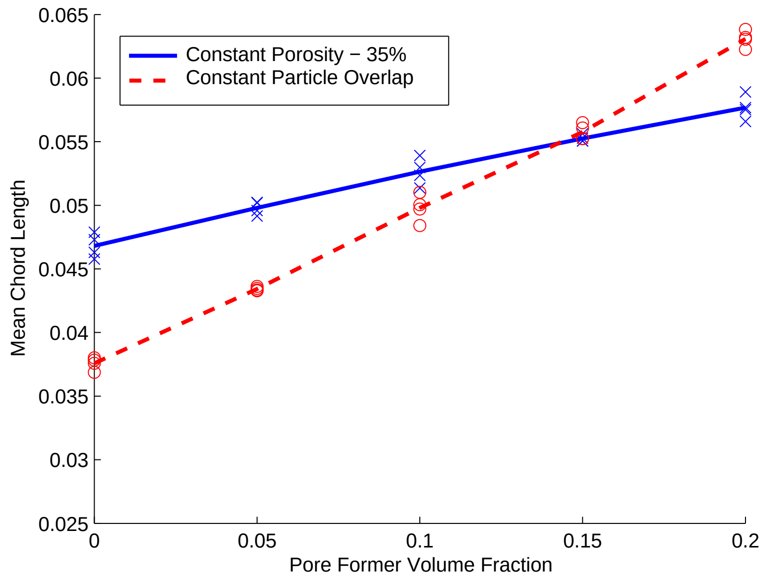

(a) Mean Chord Length

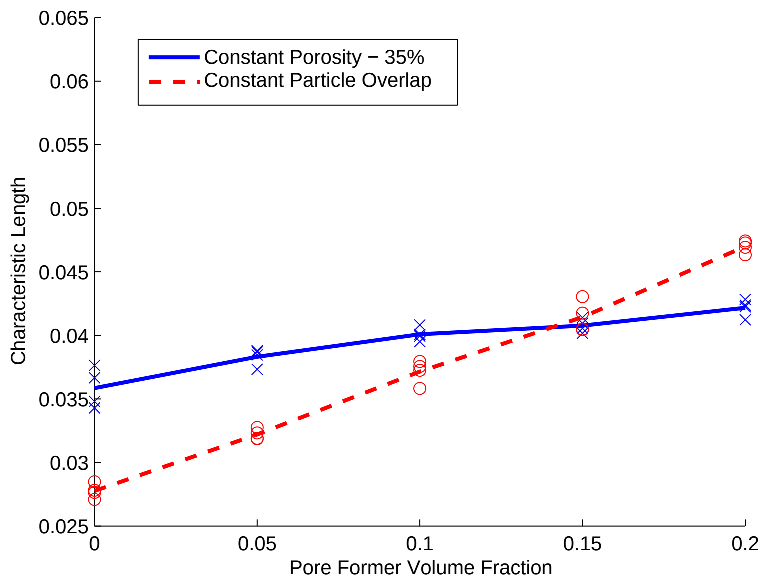

(b) Characteristic Length

Figure 5.3: Relationship between mean pore size (represented by both chord length and characteristic length) and volume fraction of pore former. All units are in relation to the domain side length of 1 and pore former particle size to solid particle size ratio is 1:1.

on the pore size.

Observation of the chord length distribution curve in Figure 5.4 reveals additional information about the nature of the pore space. The curve for the case of 0% pore former volume is a typical pore size distribution curve with a smooth exponential shape. However, when pore former particles are used, the curve develops a slight bump. This bump is very subtle at 10% pore former volume fraction but is quite clear at 20% volume fraction. The reason for this bump is simple; all pore former particles are the same size, so all pores created by these particle are of a similar size. The bump in the curve for 20% volume fraction is located at a chord length of approximately 0.075. While intuition may suggest that the bump should be located at a chord length the same approximate size as the pore former particle diameter (in this case 0.1), this does not take particle overlap into account. Just like the ion and electron conducting phases simulate a sintering effect by way of particle overlap, the pore former phase also overlaps other particles as it is placed. Therefore, the pore size carved out by a pore former particle will be smaller than the diameter of that particle (the extant of this difference depends on the magnitude of the particle overlap). The end result is that pore former particles with a diameter of 0.1 carve out pore sizes of approximately 0.075 throughout the domain.

Tortuosity

Tortuosity is related to diffusivity by equation 1.17 and if porosity is held constant, effective diffusivity is inversely proportional to tortuosity. Therefore, quantifying tortuosity is redundant since effective diffusivity will be quantified in the next section. However, it is useful to analyze tortuosity qualitatively in order to understand how a

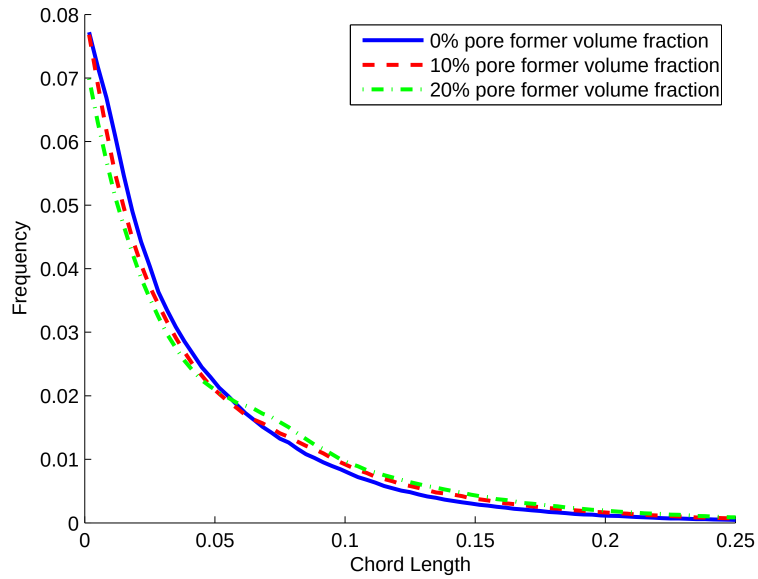

(a) Constant Porosity of 35%

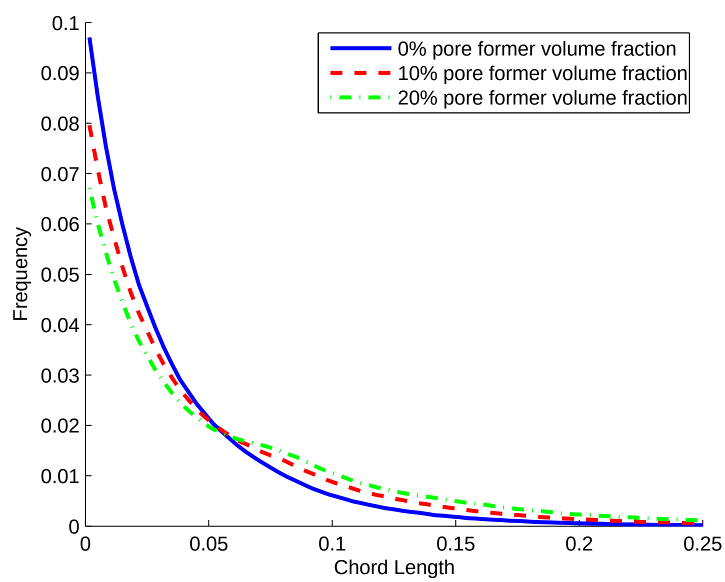

(b) Constant Particle Overlap

Figure 5.4: Chord length distribution for three different quantities of pore former volume fraction. All units are in relation to the domain side length of 1. Bin size of the distribution is 1/300.

change in tortuosity will affect effective diffusivity. Tortuosity is best observed here by looking at 2-dimensional slices of the random sphere domain. General diffusion paths can be tracked all the way through domains of many different amounts of pore former.

Figure 5.5 contains geometry slices from the case of studying the effects of pore former volume fraction with porosity held constant. Both slices contain approximately the same area of pore space but there is a clear difference in the nature of the two cases. In Figure 5.5(a) the diffusion channels are small but numerous while in Figure 5.5(b) the diffusion channels are noticeably larger but also fewer in number. If there are more channels, then the number of direct paths through the electrode is higer. The case of constant particle overlap has the same characteristics but is harder to analyze qualitatively due to the large differences in porosity.

Effective Diffusivity

Similarly to the determination of pore size distribution, diffusivity is solved using a random walk method. It can also be solved using a finite volume method (FVM) in the CFD program OpenFOAM. It is ultimately this characteristic that will determine how effective mass transport is within the electrode. Pore size distribution, porosity, and tortuosity all contribute to the effective diffusivity within a given electrode. Pore size distribution mainly contributes at very small pore sizes where Knudsen diffusion is prominent.

Like the analysis of pore size distribution, there are two cases that will be analyzed here: constant porosity and constant particle overlap. Figure 5.6 displays how effective diffusivity changes as the pore former volume fraction varies. Diffusivity is

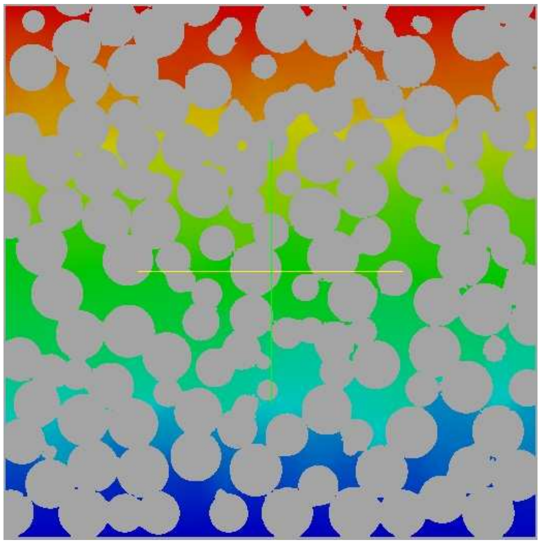

(a) 0% Pore former volume fraction

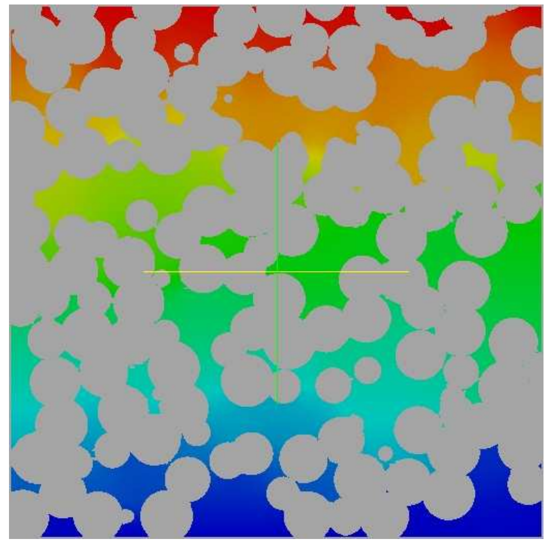

(b) 20% Pore former volume fraction

Figure 5.5: 2-dimensional slices of the 3D electrode model with varying pore former volume fraction. Porosity for both cases is 35%. The grey area represents solid phases, while the pore space is represented by a concentration gradient.

represented here as the ratio of effective diffusivity to the bulk diffusivity. The most striking difference between the two cases is the decrease in effective diffusivity with added pore former for constant porosity, and the increase for constant particle overlap. The reason for this is simple however; effective diffusivity varies with porosity. This is evident in the Bruggeman Equation (1.16) for porosities above 0.4 as well as in equation 2.1 from Berson et al. [1]. The addition of pore former appears to be the only factor affecting effective diffusivity in the case of constant porosity. In the case of constant particle overlap, the addition of pore former is joined by a changing porosity as an additional factor that will change the effective diffusivity.

It is helpful to remove the effect of porosity in this analysis so that effective

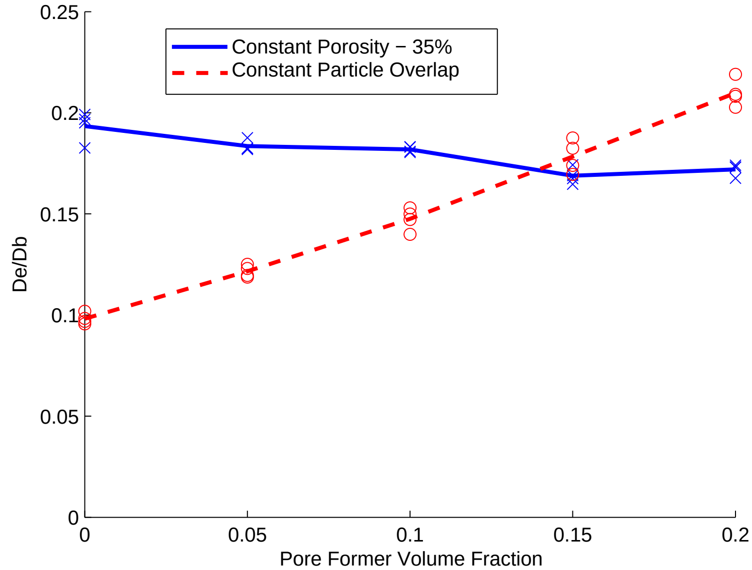

Figure 5.6: Variation of effective diffusivity, De, (represented in relation to bulk diffusivity, Db) as a function of pore former volume fraction. Average Knudsen number for all tests is $< 1/100$.

diffusivity can be compared directly to pore former volume fraction. To do this, effective diffusivity is normalized by Equation 2.1 for both cases. It is important to note that for both Figures 5.6 and 5.7, a length scale was chosen so that Knudsen effects would be almost non-existent. The average Knudsen Number in each test was less than $1/100$. This almost completely eliminates the effects of mean pore size on the effective diffusivity. While Figure 5.6 displays the effects of porosity and tortuosity on diffusivity, Figure 5.7 illustrates how the diffusivity is affected by only the tortuosity change brought upon by an increase in pore former volume fraction. With the effect of porosity removed, both cases show the same trend of diminishing diffusivity with added pore former. This relationship is expected because the diffusion paths were qualitatively shown to become more tortuous as a greater amount of pore former is included in the electrode.

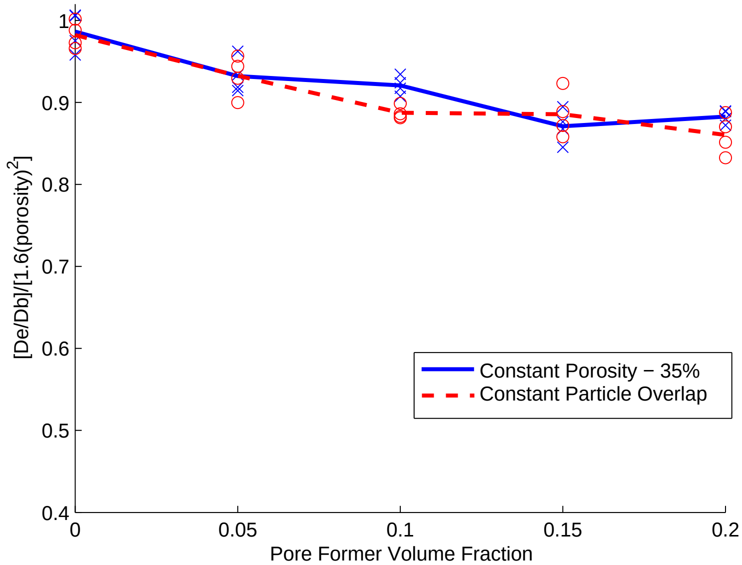

Figure 5.7: Effective diffusivity, De/Db, normalized to the expected theoretical result (equation 2.1).

The effect of tortuosity as a result of added pore former is not the only factor worth isolating. The analysis of pore size distribution and how it changes with pore former volume fraction was done in Section 5.1.1. The Bosanquet correlation demonstrates how effective diffusivity will then be altered by these changes in the pore size distribution. Figure 5.8 is a re-creation of Figure 2.2 taken from Berson et al. [1] but with one difference, the simulations were tested on a geometry that contained 20% pore former volume fraction.

The final series of tests will use a realistically sized electrode geometry to determine the effects of both tortuosity and pore size at the same time. The diffusivity will be normalized by Equation 2.1, as was done in Figure 5.7, to neglect the effect of porosity.

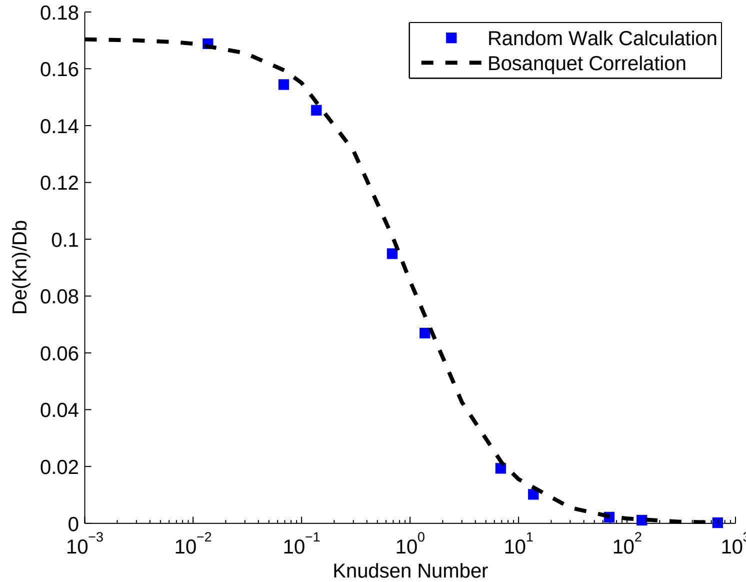

Figure 5.8: Graphical representation of the Bosanquet correlation and of diffusivity determined by the random walk simulation for varying Knudsen numbers.

The domain side length was set to $10\mu m$ and each solid particle had a diameter of $1\mu m$. The electrode was assumed to be a cathode, with oxygen as the diffusing gas having a mean free path of approximately $0.25\mu m$. Figure 5.9 displays the results of this diffusion simulation for a realistically sized cathode geometry.

The most striking difference between Figure 5.9 and Figure 5.7 is the translation of the data from a diffusivity near what is expected from Equation 2.1 to a $[De/Db]/[1.6\varepsilon^2]$ near 0.5. This change is due to the mean pore size of the realistic electrode model. The Knudsen number for each geometry is located in the transition diffusion regime; specifically between 0.5 and 1.0. The Bosanquet correlation, as seen in Figure 5.8, states that at a Knudsen number of 1, effective diffusivity will be half what is expected for $[De/Db]_{Kn\rightarrow 0}$. Another difference between Figures 5.7 and 5.9 is

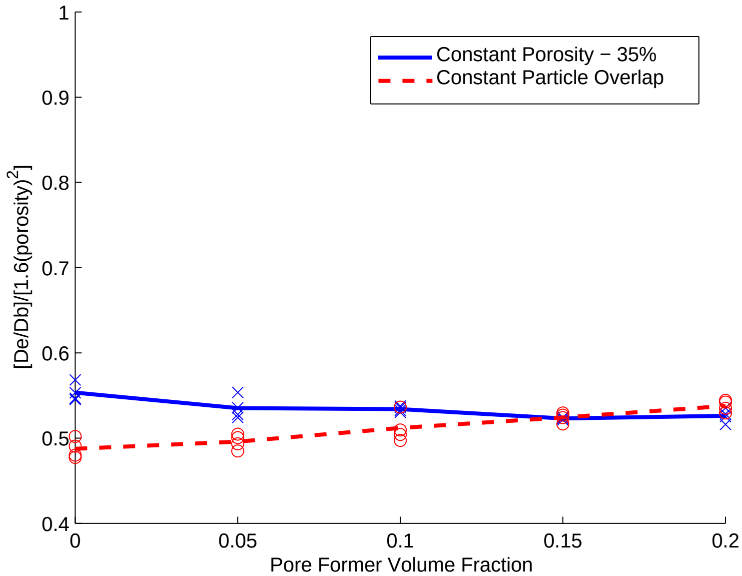

Figure 5.9: Effective diffusivity, De/Db, normalized to the expected theoretical result for a realistically sized electrode.

the lack of a clear downward trend in the latter figure. $[De/Db]/[1.6\varepsilon^2]$ in Figure 5.7 varies by as much as 0.12, while in Figure 5.9 it varies by less than 0.05 for both cases. What is more, the case of constant porosity seems to trend downward slightly while the case of constant overlap trends upward slightly. These results demonstrate that the addition of pore former increases tortuosity (negative effect on De) and increases pore size (positive effect on De). In the case of constant porosity, altering tortuosity has a greater impact than altering pore size. In the case of constant particle overlap, pore size has a greater impact than tortuosity because mean pore size increases more rapidly with pore former volume fraction as evidenced in Figure 5.3. In general, the two effects almost cancel each other and for the realistic geometry presented, altering pore former volume fraction will not significantly affect effective diffusivity.

5.1.2 Effect of Altering Pore Former Particle Size

In the following tests, the particles of each separate phase (ion and electron conducting, and pore former) are mono-sized, but the pore former particles are not necessarily the same size as the charge carrying particles. An initial series of tests of pore former particle size used seven different particle sizes. They were, in relation to the size of the electron and ion conducting particles, 0.625, 0.714, 0.833, 1.0, 1.2, 1.4, and 1.6. The final series of tests of the pore former particle size used these same values as well as smaller sizes of 0.55, 0.50, 0.42, and 0.36. Like in Section 5.1.1 the domain was constructed using the random sphere dropping program with pore former included. Unlike Section 5.1.1, as pore former size is changed, neither the porosity nor the particle overlap needs to vary to make space. A porosity of 35% and a pore former volume fraction of 0.1 were used for all tests in this section.

Figure 5.10 contains two 3-dimensional porous domains with differing sizes of pore former particles used. The change in size of the pore former particle will have an effect on the microstructural properties of the domain as will be seen in the following sections. However, from a simple inspection of the domains in Figure 5.10, there is no visible difference between each case as neither the porosity nor the particle overlap is changing.

Pore Size Distribution

Mean pore size is quantified here by again employing the random walk method of collecting chord lengths. Since neither porosity nor particle overlap need to vary with a changing pore size, there is only one relationship to analyze in this section. Figure 5.11 illustrates the relationship between the mean pore size (represented by

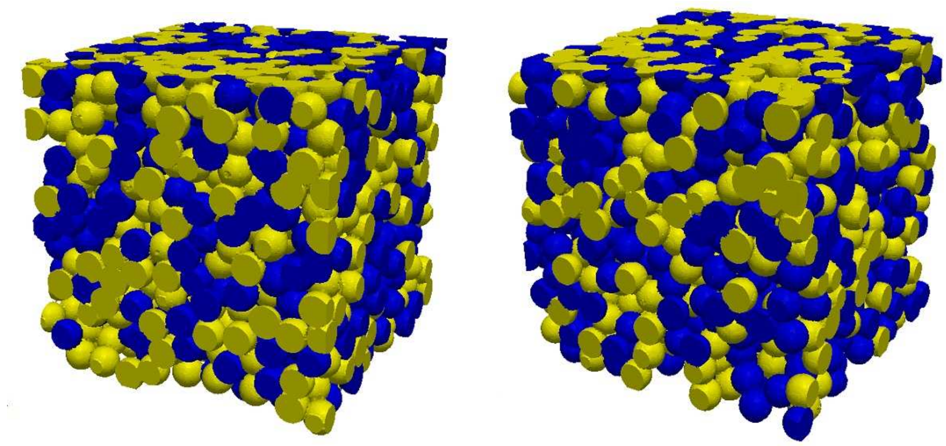

(a) Pore former particle size of 0.36 (b) Pore former particle size of 1.6

Figure 5.10: 3D model of a $10\mu m \times 10\mu m \times 10\mu m$ section of SOFC electrode created with different sizes of pore former particles. Porosity is 35% and pore former volume fraction is 0.1.

both chord length and characteristic length) and pore former particle diameter. As before, the length scale used in this analysis sets the side length of the domain to a standard unit size of 1. All electron and ion conducting particles are of a diameter of 0.1. It is expected that by placing a larger pore former particle, the mean pore size will increase. This is exactly what happens, but the increase in mean pore size is small in comparison to the increase in pore former particle size. For example, a pore former particle diameter of 0.05 results in a characteristic length of 0.037 (CL is 74% of the particle diameter). However, a pore former particle diameter of 0.16 results in a characteristic length of only 0.046 (CL is 29% of the particle diameter). A closer examination of the chord length distributions will provide insight into this.

Figure 5.12 displays the chord length distributions for structures built with 3 different pore former particle sizes. The differences between cases in this instance are

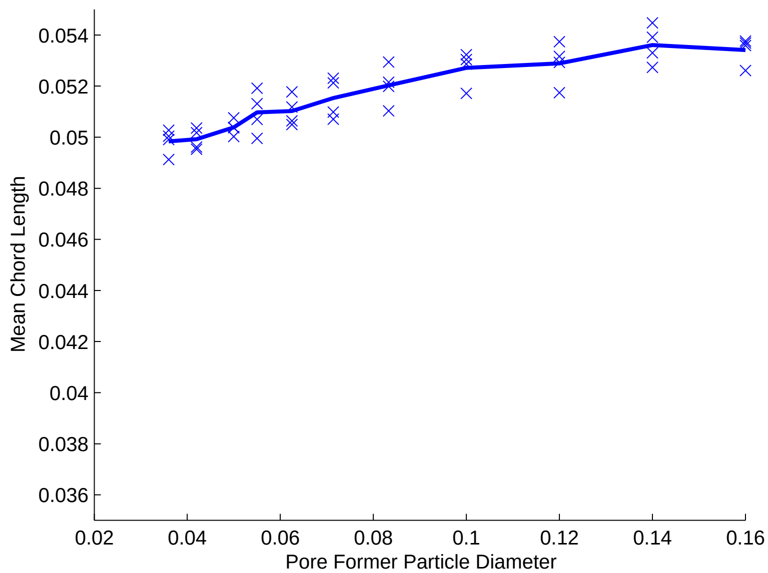

(a) Mean Chord Length

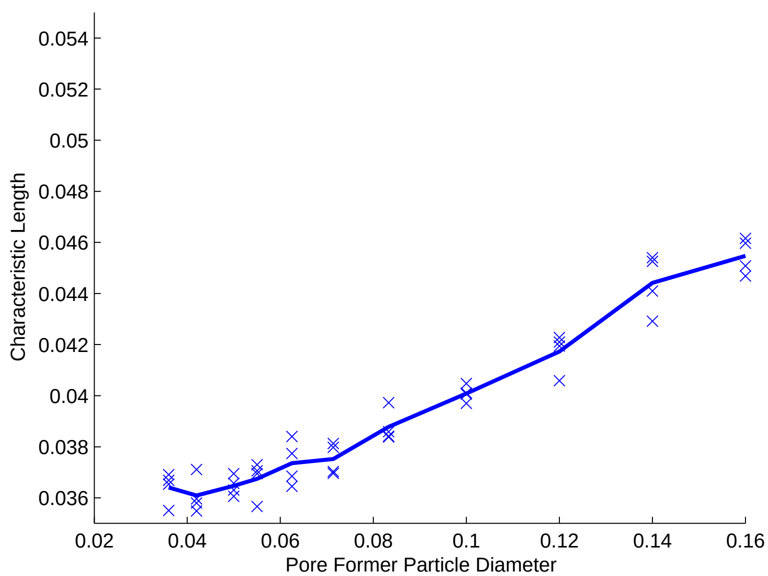

(b) Characteristic Length

Figure 5.11: Relationship between mean pore size (represented by both chord length and characteristic length) and pore former particle diameter. Porosity is 35% and pore former volume fraction is 0.1. All results are in ratio to a domain side length of 1.

less drastic than in section 5.1.1. Though the differences are subtle, they tell us a lot about the pore space. The case of 0.036 particle size has the greatest number of pores within the size range of approximately 0.02 to 0.055. The structure with 0.083 pore former particle size has the greatest number of pores within the size range of approximately 0.06 to 0.11. And finally, the case of 0.16 particle size has the greatest frequency of pores bigger than 0.13 as well as pores smaller than 0.015. It is not surprising that for each case, the bulge in the pore size distribution curve is located right around the pore former particle diameter for that case. What is interesting is that the case with the largest pore former particle size has the greatest frequency of tiny pores (< 0.015). This can be explained by the number of pore former particles dropped in each case. Since all cases have the same pore former volume fraction, cases with a larger particle diameter will have fewer total pore former particles. For example, the 0.16 diameter particle has 7.1 times more volume than the 0.083 diameter particle; resulting in approximately 7.1 times fewer particles being dropped in the domain. In this building algorithm, pores are created by pore former particles as well as being naturally created without them (as evidenced by the case of 0% pore former). Tiny pores (< 0.015) can only be created naturally and not by pore former (no case here uses pore former particles that small). Therefore, the case using 0.16 diameter pore former particles has far fewer pores created by pore former in proportion to the number of pores created naturally. This doesn't mean there is a greater number of total tiny pores compared to other cases, but rather that it has a greater percentage of tiny pores since there are fewer pores created by pore former particles.

In Figure 5.3 in Section 5.1.1 the characteristic length is only different from chord length in magnitude, while in Figure 5.11 the characteristic length has an obviously

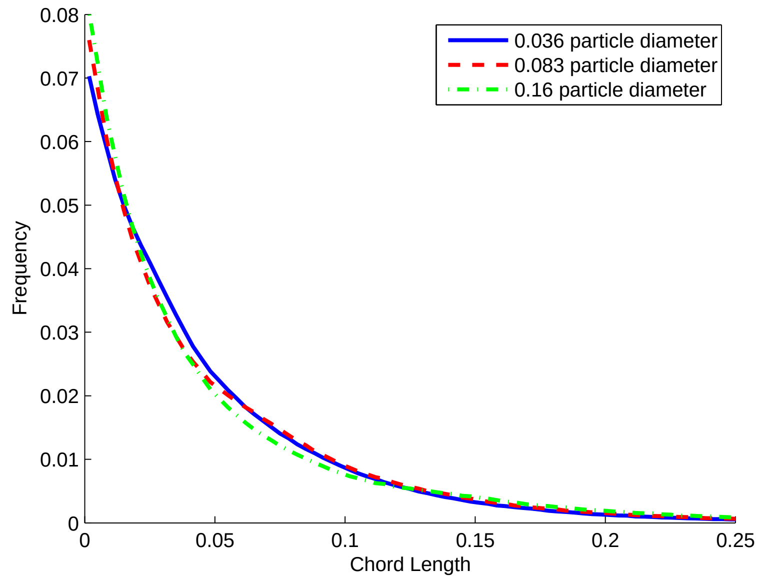

(a) Linear Scale

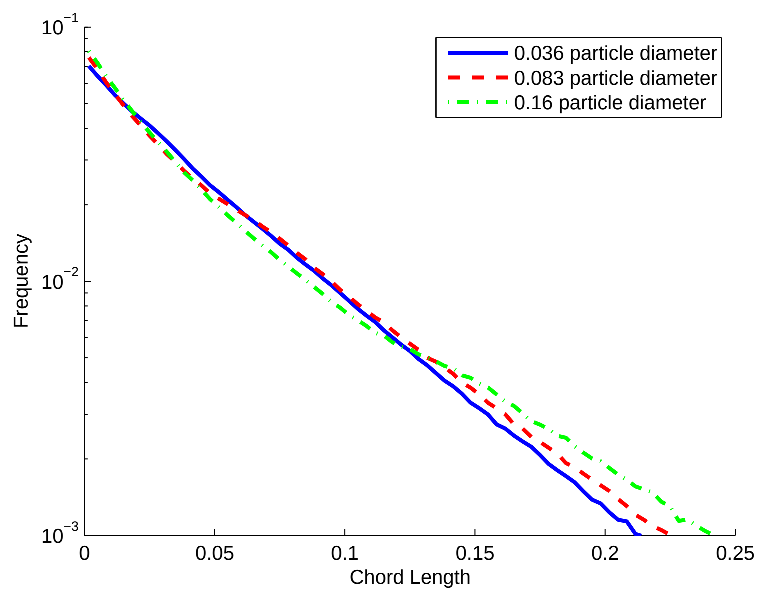

(b) Logarithmic Scale

Figure 5.12: Chord length distribution for domains constructed with 3 different pore former particle diameters. Porosity is 35% for all cases and all units are in relation to the domain side length of 1. Bin size of the distribution is 1/300.

larger slope, especially at pore former particle sizes of 0.1 and higher. Inspection of equation 4.1 provides an explanation. Random isotropic packings of spheres are expected to have an exponential chord distribution and the term $\langle l^2 \rangle / 2\langle l \rangle^2$ should then equal 1 [34]. Berson et al. [1] showed that for this model, $\langle l^2 \rangle / 2\langle l \rangle^2$ is slightly larger than 1 (approximately 1.07 for monodisperse structures). Berson et al. concluded this was because the domain was non-isotropic due to the constructing algorithm of dropping spheres. In Section 5.1.1 the term $\langle l^2 \rangle / 2\langle l \rangle^2$ remained between 1.07 and 1.10 with no apparent dependance on pore former volume fraction. Figure 5.13 displays how this term behaves in the analysis of pore former particle size.

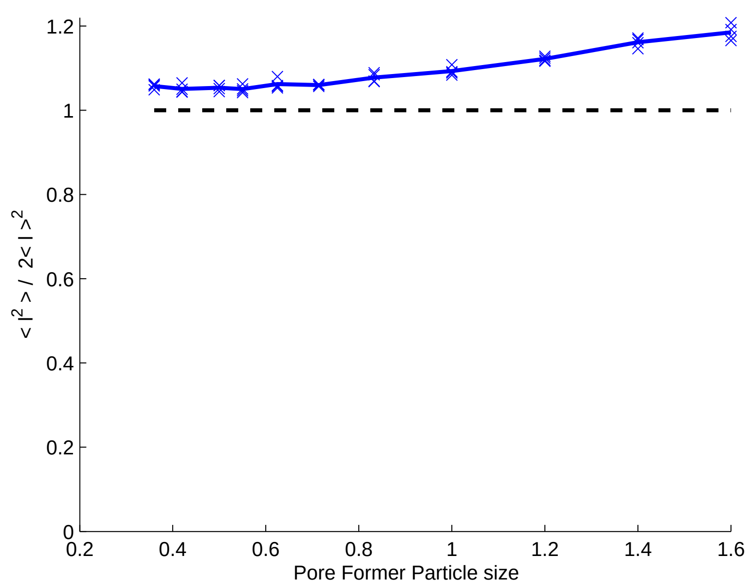

Figure 5.13: $\langle l^2 \rangle / 2\langle l \rangle^2$ as a function of pore former particle size. The dashed line represents the expected value of 1 for an exponential distribution of chords.

When large pore former particles are used instead of small particles or no particles at all, the shape of the pore space is changed drastically and therefore $\langle l^2 \rangle / 2\langle l \rangle^2$ grows further from unity. Inspection of Figure 5.12(b) provides additional evidence that the 0.16 distribution is not exponential (an exponential distribution should have a straight line).

Tortuosity

The analysis of tortuosity for this section is done in the same way as in Section 5.1.1. Figure 5.14 displays two slices from separate electrode domains that use different pore former particle sizes. The two extreme cases of pore former size (0.036 and 0.16) are presented. Much like an increase in pore former volume fraction, an increase in pore former particle size has a detrimental effect on tortuosity. Phase segregation is far more evident in Figure 5.14(b) than what can be seen in Figure 5.14(a). Although the diffusion paths are smaller, a greater number of paths are formed when a smaller pore former particle is dropped.

Effective Diffusivity

Once again, effective diffusivity is analyzed by determining the effects of tortuosity and pore size separately. There is no analysis here on the effects of porosity on effective diffusivity as Berson et al. [1] previously analyzed this in SOFC electrodes. Figure 5.15 illustrates the relationship between pore former particle size and effective diffusivity for $Kn \to 0$. Low Knudsen number diffusion is used again to negate the effects of pore size and isolate the effects of tortuosity. Similarly to an increase in pore former volume fraction, an increase in pore former particle size is detrimental to diffusivity. The magnitude of this effect is approximately the same here as it was in Figure 5.6. At 35% porosity, a domain constructed of 0.2 pore former volume fraction

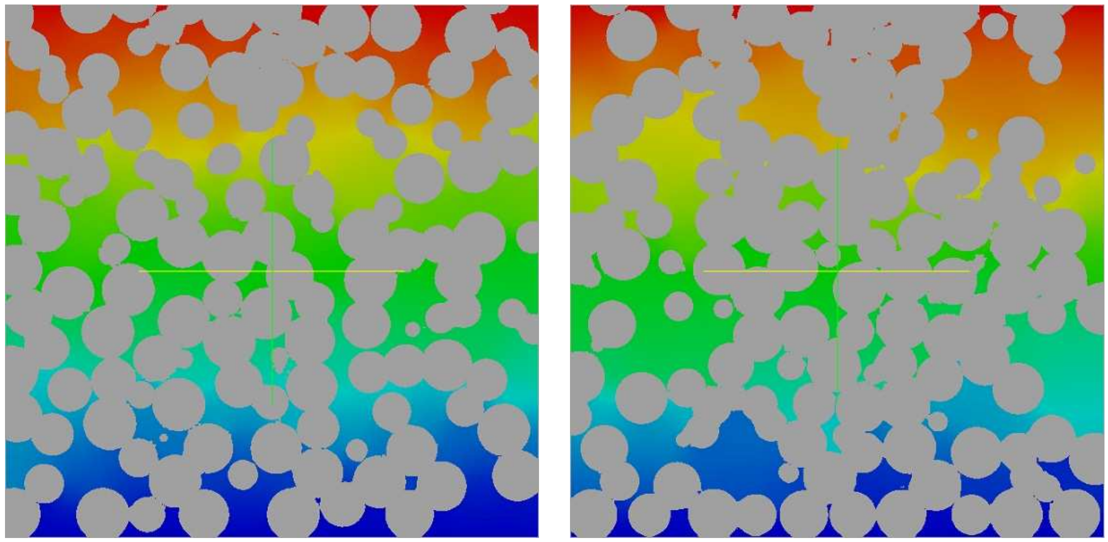

(a) 0.036 Pore former particle size (b) 0.16 Pore former particle size

Figure 5.14: 2-dimensional slices of the 3D electrode model with varying pore former particle size. Porosity for both cases is 35% and pore former volume fraction is 0.1. The grey area represents solid phases, while the pore space is represented by a concentration gradient.

and a pore former particle diameter of 0.1 yields a similar effective diffusivity to a domain constructed of 0.1 pore former volume fraction and a pore former particle diameter of 0.16. When the pore former particle size becomes small (approaches 0), the effective diffusivity approaches a similar value that results from using no pore former at all.

The Bosanquet correlation (Equation 1.20), which was analyzed in Figure 5.8 is applicable again in this section. An increase in mean pore size, brought upon by an increase in pore former particle size, should increase the effective diffusivity. The question is how much will this increase be in comparison to the decrease in diffusivity brought upon by an increasing tortuosity. Once again, a realistically sized electrode

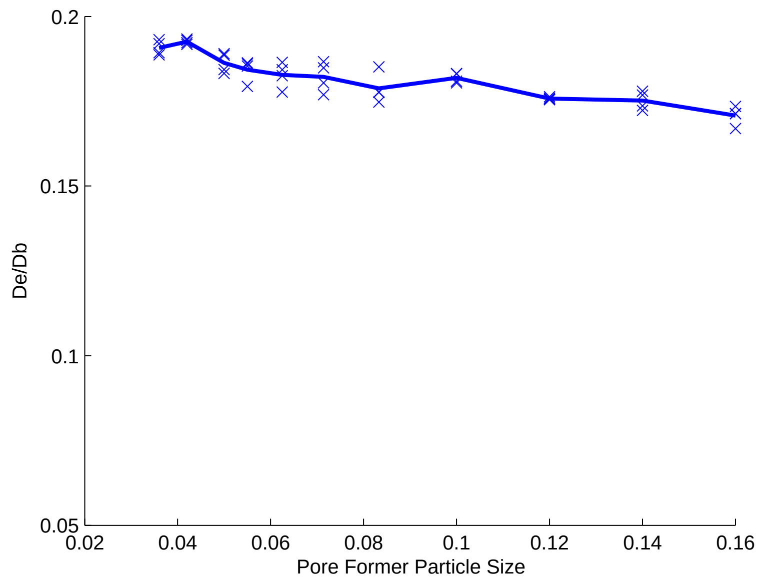

Figure 5.15: Variation of effective diffusivity, De, (represented in relation to bulk diffusivity, Db) as a function of pore former particle size. Average Knudsen number for all tests is $< 1/100$ and porosity is 35%.

domain is investigated in order to determine the effects of both pore size and tortuosity together. The domain side length is again set to $10\mu m$ while the solid particle size and mean free path are $1\mu m$ and $0.25\mu m$ respectively.

Figure 5.16 displays the behavior of effective diffusivity in a realistically sized electrode for domains constructed with various pore former particle diameters. Again, the primary consequence of using a realistically sized electrode is the reduction in magnitude of the effective diffusivity due to Knudsen effects. De/Db ranges from 0.193 to 0.171 when Knudsen effects are ignored, while De/Db ranges from 0.111 to 0.098 for a realistically sized domain. In Figure 5.16, there is a definite downward trend to diffusivity as pore former particle size increases. This downward slope is not as pronounced as what occurs in Figure 5.15 and this can be attributed to the

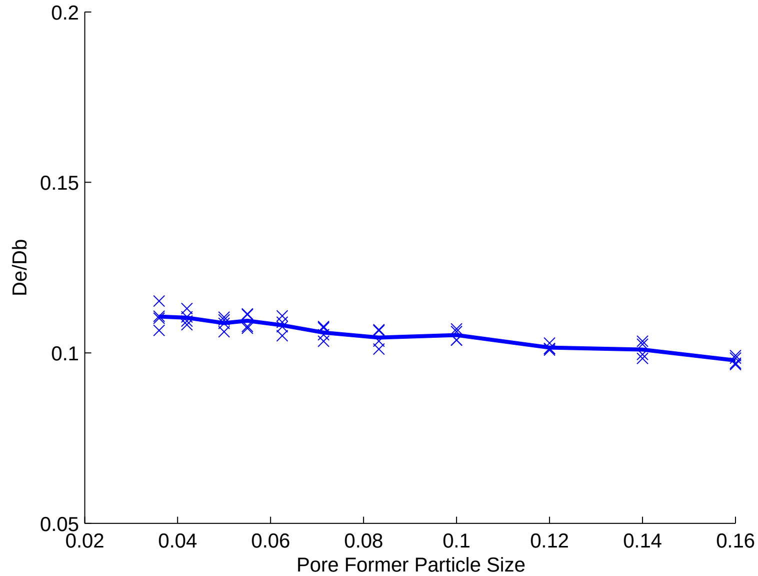

Figure 5.16: Variation of effective diffusivity, De, (represented in relation to bulk diffusivity, Db) as a function of pore former particle size for a realistically sized geometry. Porosity is 35% and pore former volume fraction is 0.1.

increasing mean pore size (and therefore less Knudsen effects) as pore former particle size increases. However, the fact that the diffusivity decreases goes to show that the consequences of tortuosity outweigh the benefits of mean pore size when using a larger pore former particle diameter. It is important to note that this trend may only apply for the characteristics tested here (specifically $1\mu m$ solid particle size at 35% porosity).

5.2 Dropping Solid Agglomerates

The main purpose of using solid agglomerates is to better simulate the structure of a realistic fuel cell electrode. The purpose of the following tests is to determine the difference between using two pre-agglomerated solid phases, one pre-agglomerated solid phase, and no pre-agglomerated solid phases (also referred to as two single sphere phases). The same three characteristics as the sections above are analyzed: pore size distribution, tortuosity, and diffusivity. Also examined was how all of these characteristics changed with porosity for each of the three cases.

Isometric views of the sample electrode model are presented in Figure 5.17. The distinction here between the two cases is greater than any other isometric view in the previous sections. Figure 5.17(a) was constructed using previously established techniques and is clearly a domain filled with barely overlapping spheres. Figure 5.17(b) was constructed using pre-agglomerated particles and while it also clearly consists of spheres, there is a large amount of particle overlap and phase segregation that appears to better represent a domain of non-spherical irregular shapes. A qualitative comparison of both cases with an FIB-SEM reconstruction (such as Figure 2.1) suggests Figure 5.17(b) may be a closer match.

5.2.1 Pore Size Distribution

It is known that the mean pore size of a solid porous domain increases as porosity increases. As displayed in Figure 5.18 the linear relationship between mean pore size and porosity does exist for each of the three cases mentioned in the section above. Due to restrictions of the particle placing algorithm, the upper limit of porosity for the case of no agglomerates is approximately 40% to 44%. Likewise, due to the difficulty of closely packing pre-agglomerated particles, the lower limit of porosity for the case of both phases agglomerated is approximately 30%.

The slope of the lines are approximately equal for each case, while the magnitudes of the mean pore size are different. In terms of a domain side length representing a

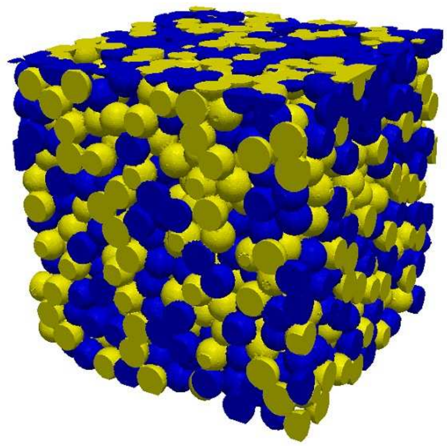

(a) Both phases constructed with single spheres

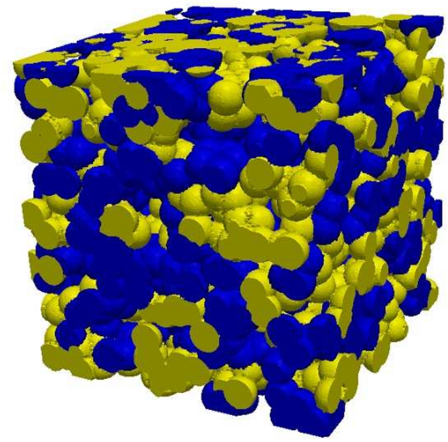

(b) Both phases constructed with pre-agglomerated particles

Figure 5.17: 3D model of a $10\mu m \times 10\mu m \times 10\mu m$ section of SOFC electrode. Porosity is 30% for both cases.

unit size of 1, the case of one 'pre-agglomerated solid phase' contains pore sizes which are approximately 0.011 units larger than when both phases contain single spheres. Likewise, the case of both solid phases pre-agglomerated contains pore sizes approximately 0.026 units larger than when both phases contain single spheres. An increase in pore size can be attributed to the fact that the agglomerate of four spheres can be thought to represent one irregular shaped particle rather than four joined spherical particles. If two domains are created, both with mono-sized spherical particles but the particle size of one domain is twice as large as the other, then the mean pore size will also be approximately twice as large. The same principal applies here as an agglomerate particle made of four spheres is certainly larger than a particle made from a single sphere.

The pore size distribution of all three cases is illustrated in Figure 5.19. As

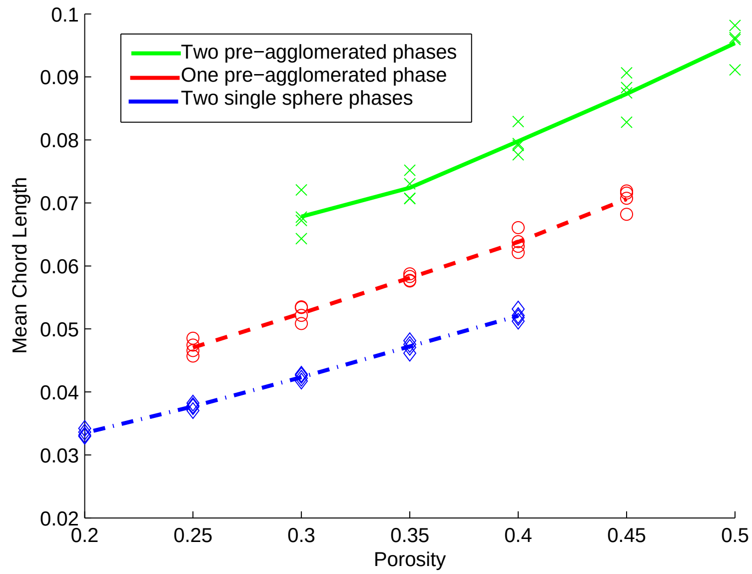

(a) Mean Chord Length

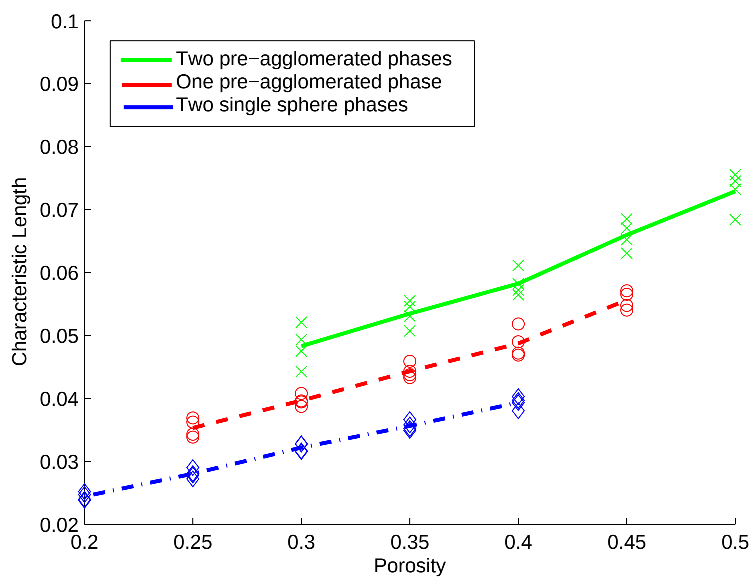

(b) Characteristic Length

Figure 5.18: Relationship between mean pore size (represented by both chord length and characteristic length) and porosity of a domain created with Agglomerates. All results are in ratio to a domain side length of 1.

expected, the case of two pre-agglomerated phases has a higher frequency of large pores and a lower frequency of small pores than the other two cases. Conversely, the case of two single sphere phases has a higher frequency of small pores and and a lower frequency of large pores than the other cases. The frequency of all cases intersect at a pore size of approximately 0.058. All distributions have a smooth, exponential curve, with no cases developing a bump as was seen in the distributions when pore former was used (Figure 5.4).

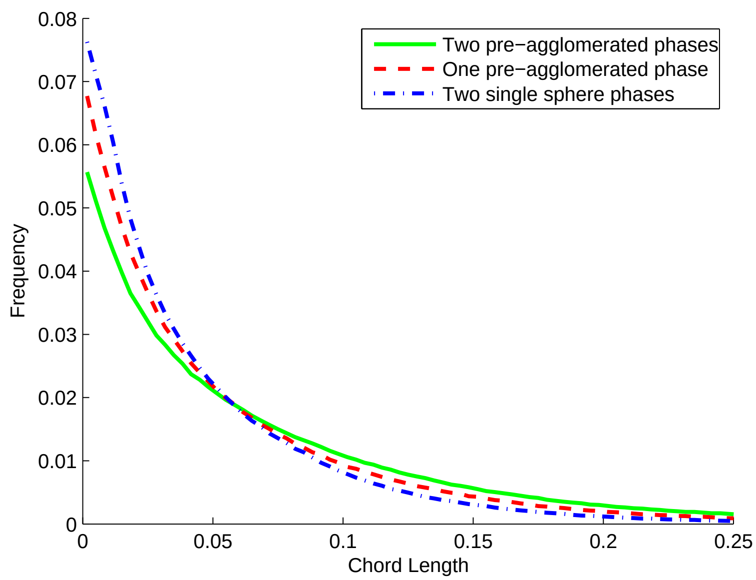

Figure 5.19: Chord length distribution for the three cases of this study. Porosity is 35% for all cases and all units are in relation to the domain side length of 1. Bin size of the distribution is 1/300.

5.2.2 Tortuosity

Analysis of tortuosity for pre-agglomerated particles will again be done in a qualitative manner. Figure 5.20 represents the cases of the old ‘single sphere’ algorithm and the new ‘pre-agglomerated’ algorithm. The contrast between the cases is stark. Figure 5.20(a) is very similar to other slices seen in Section 5.1 as the pore space consists of many small flow channels. Figure 5.20(b) shows more phase segregation than any structure created with pore former particles. Using two pre-agglomerated phases also seems to create larger, but fewer, diffusion paths similarly to what was seen with a high pore former volume fraction or a large pore former particle size. Like the cases involving pore former, the tortuosity of the case with two pre-agglomerated phases will be higher than that of two single sphere phases.

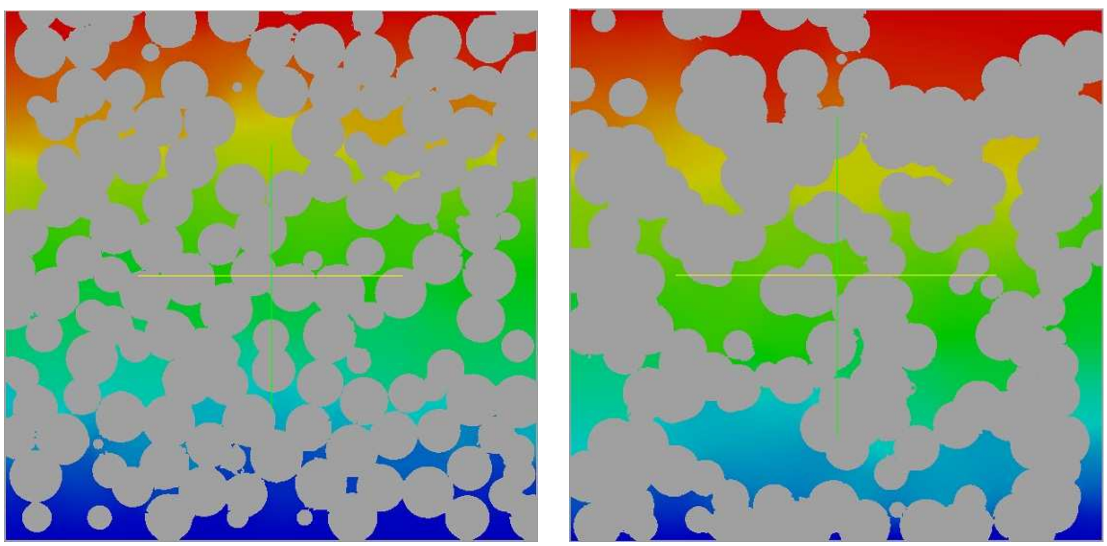

(a) Two single sphere phases

(b) Two pre-agglomerated phases

Figure 5.20: 2-dimensional slices of the 3D electrode model with both the single sphere algorithm and the pre-agglomerated particle algorithm. Porosity for both cases is 30%. The grey area represents solid phases, while the pore space is represented by a concentration gradient.

5.2.3 Effective Diffusivity

The purpose of building a domain with pre-agglomerated particles is to better represent the shape of an actual fuel cell electrode. If these domains do indeed better represent an actual fuel cell then the resulting effective diffusivity from the following tests should also better represent what occurs in a real electrode. The potential inaccuracies in diffusivity from using the old random sphere domains are possibly exposed here. The random walk algorithm for solving diffusivity used before is applied again for the following tests.

Figure 5.21 illustrates how effective diffusivity changes with porosity for the three cases tested: Two pre-agglomerated phases, one pre-agglomerated phase, and no pre-agglomerated phases. Knudsen effects are ignored initially to isolate the impact of tortuosity. In Figure 5.21(a) De/Db is represented versus an increasing porosity, and in all cases diffusivity increases as expected. The case of no pre-agglomerated phases (or two single sphere phases) should follow the $1.6\varepsilon^2$ trend as demonstrated in Berson et al. [1]. The behavior of the other two cases is distinctly different suggesting that the $1.6\varepsilon^2$ trend doesn't apply to a geometry created with pre-agglomerated particles. Figure 5.21(b) allows a closer examination of this by normalizing De/Db to $1.6\varepsilon^2$. The case with two single sphere phases demonstrates a near horizontal line at unity; the slight downward slope suggests that equation 2.1 does not perfectly fit the data but is extremely close. The two cases involving pre-agglomerated particles are not close to unity with both cases falling between 0.93 and 0.81. The likely cause of this discrepancy is the fact that tortuosity appears to increase when pre-agglomerated particles are used (as seen in section 5.2.2) when compared to the old single sphere algorithm. Also, with both phases pre-agglomerated, and to a lesser extant one phase pre-agglomerated, the downward slope of the line in Figure 5.21(b) is decidedly more pronounced. This indicates that equation 2.1 does not adequately describe the relationship between diffusivity and porosity when the domain is constructed with pre-agglomerated particles.

The construction of a realistically sized electrode domain will allow the effects of mean pore size on diffusivity (Figure 5.8) to be analyzed along side the effects of tortuosity on diffusivity (Figure 5.21). Like before, the domain side length used for testing is $10\mu m$, the solid particle diameter is $1\mu m$, and the mean free path is $0.25\mu m$. Figure 5.22 displays the effective diffusivity results from a realistically sized electrode as a ratio to equation 2.1.

Each of the three cases - two pre-agglomerated phases, one pre-agglomerated phase, and no pre-agglomerated phases - display very distinct relationships for effective diffusivity versus porosity. The old single dropped sphere algorithm will be discussed first with its results becoming the benchmark for the other two cases. In Figure 5.21(b), $[De/Db]/[1.6\varepsilon^2]$ did not vary significantly with porosity, but in Figure 5.22, there is a clear upward trend of $[De/Db]/[1.6\varepsilon^2]$ with porosity. This is completely due to an increasing mean pore size and demonstrates that equation 2.1 does not consider Knudsen effects (nor does Bruggeman's equation). The case with one pre-agglomerated phase actually shows a similar trend to no pre-agglomerated phases in this test. When one pre-agglomerated phase is used for construction, both mean pore size (helpful to De) and tortuosity (not helpful to De) were shown to be higher. But when these factors are combined in a realistically sized domain, their differences balance out and the diffusivity versus porosity relationship is nearly the same as the case of no pre-agglomerated particles. That the case of one pre-agglomerated

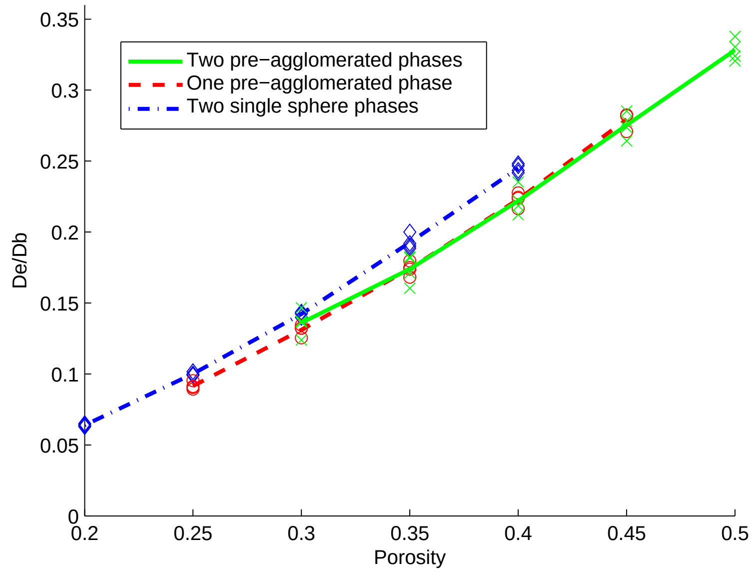

(a) Effective Diffusivity

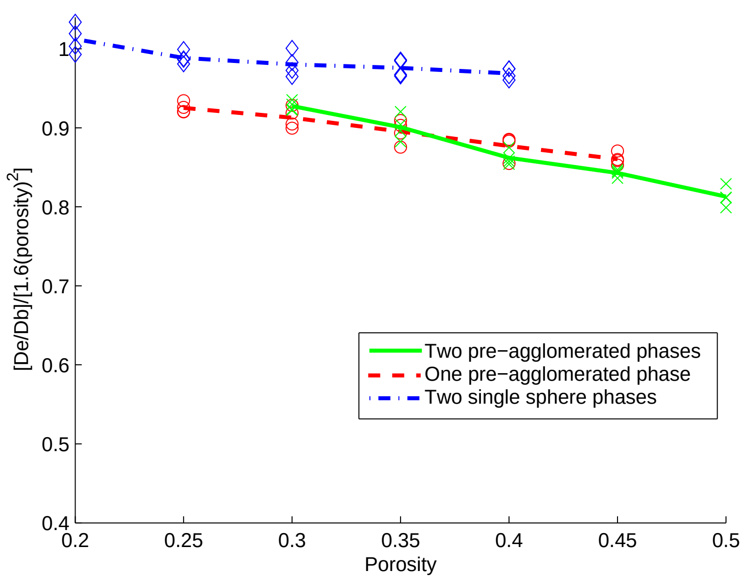

(b) Effective Diffusivity normalized to $1.6\varepsilon^2$

Figure 5.21: Diffusivity as a function of porosity for various levels of pre-agglomerated particle use.

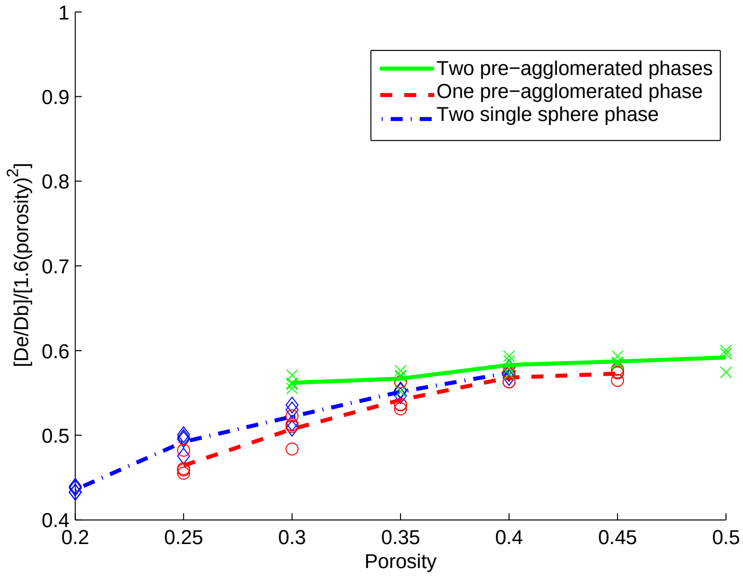

Figure 5.22: Diffusivity normalized to $1.6\varepsilon^2$ as a function of porosity for a realistically sized electrode with pre-agglomerated particles.

phase provides slightly lower diffusivities suggests that the tortuosity has greater influence than mean pore size. The case with two pre-agglomerated phases shows a different trend than what appears for the single spheres case. Again, the difference in tortuosity and the difference in mean pore size balance each other, but in this case De is slightly higher, suggesting mean pore size has greater influence than tortuosity. Also, Figure 5.22 demonstrated that equation 2.1 may not adequately describe the relationship between effective diffusivity and porosity for a domain constructed with pre-agglomerated particles. This error is translated to Figure 5.21(b) as the slope of the line for two pre-agglomerated phases is noticeably shallower than the case of no pre-agglomerated particles.

Chapter 6

Summary and Conclusions

6.1 Summary

This thesis involved the examination of changes made to the standard randomly packed spheres electrode micromodel and their effects on gas diffusivity within said electrode. The analysis of diffusivity was broken down into three structural characteristics that greatly impact effective diffusivity: pore size distribution, tortuosity, and porosity. There were two changes made to the standard randomly packed spheres model: the ability to drop pore former particles, and the ability to place pre-agglomerated particles.

Methods for measuring pore size distribution were investigated closely in Chapter 4. As an additional goal, a novel method for measuring pore size locally for the purpose of determining a local Knudsen number was proposed. Using a random walk technique, mean pore size is measured by collecting a distribution of chords and using equation 4.1 to determine a characteristic length. Tortuosity was analyzed qualitatively by viewing 2-dimensional slices of the electrode domain created with the CFD program OpenFOAM and the visualization tool Paraview. Diffusivity is analyzed using a random walk algorithm very similar to the one used for pore size analysis. Effective diffusivity is determined with and without Knudsen effects.

The effect of placing pore former particles was gauged in two ways: the variation of pore former volume fraction and the variation of pore former particle size. The effect of using pre-agglomerated particles was gauged by comparing three cases with each other: two pre-agglomerated phases, one pre-agglomerated phase, and no pre-agglomerated phases. Relationships between characteristic length/effective diffusivity and porosity were determined for each case.

6.2 Conclusion

The primary goal of this research was to develop a better 3D model of randomly packed spheres by adding two new features. Effective diffusivity was analyzed for both of these features to gauge their impact. As pore former volume fraction increases, so too does both mean pore size and tortuosity. A high mean pore size has a positive effect on diffusivity due to reduced Knudsen effects while a high tortuosity has a negative effect on diffusivity. These effects generally balanced as effective diffusivity decreased slightly with pore former volume fraction at constant porosity (35%) but effective diffusivity increased slightly with pore former volume fraction at constant particle overlap.

When pore former particle size is increased, mean pore size and tortuosity will also increase. Like the tests for pore former volume fraction, the effects of mean pore size and tortuosity on diffusivity somewhat balance. However, for the case tested in this research (35% porosity and $1 \mu m$ solid particle diameter) the effects of tortuosity had more influence than the effects of mean pore size and effective diffusivity decreased slightly with an increasing pore former particle size.

Placing pre-agglomerated particles instead of single spherical particles proved to alter the microstructure of the electrode domain and therefore had consequences on the effective diffusivity. Dropping pre-agglomerated particles caused the mean pore size to increase in comparison to dropping single spheres. Tortuosity also appeared to increase when pre-agglomerated particles were implemented. In addition, the effective diffusivity of domains constructed with pre-agglomerated particles does not appear to follow equation 2.1 [1]. The purpose of using pre-agglomerated particles is to more accurately model a real SOFC electrode. If the model presented here is indeed more accurate, then this research suggests that results provided by simple randomly packed spheres models are not sufficient.

The final goal of this research was to introduce a new technique for determining pore size that allows the measurement of pore size at a local scale within the electrode. A method was proposed and compared to the random walk technique used for characterization of the new model features. Characteristic length was shown to match nicely, but this was mostly by chance as the mean chord length $\langle l \rangle$ and ratio of moments $\langle l^2 \rangle / 2\langle l \rangle^2$ were both inaccurate. Ultimately, the current form of this method is not yet suitable for determining pore size either at a local level or for the entire domain.

6.3 Future Work

A logical next step for this research is to determine the effects of both pore former particles and pre-agglomerated particles on other important properties within a fuel cell electrode including electronic conductivity, ionic conductivity, and triple phase boundary length. Also, the purpose of adding pore former and pre-agglomerated particles was to add realism to the standard packed spheres model. Qualitative evidences suggested this to be true, but for sufficient verification, quantitative evidence must be provided. To accomplish this, computational domains reconstructed with FIB-SEM or XCT techniques should be tested for diffusivity and pore size distribution in the same manner as was used in this work. Quantitative comparison between reconstructed geometries and the results from this work would demonstrate the effectiveness of using pore former and pre-agglomerated particles.

The work presented here on pre-agglomerated particles uses only one geometric configuration (4 spheres). It would be helpful to test additional configurations of agglomerates with varying numbers of particles attached. Perhaps even better would be the altering of the particle placing algorithm to randomize the agglomerate geometry each time a new pre-agglomerated particle is dropped. A potential benefit of using agglomerates is that they can mimic other shapes by using enough spheres. For instance, if one wanted to capture the effect of plasma sprayed electrodes, which consists of disk shaped particles due to splattering, a number of spheres could be arranged in a pattern that resembles a disk.

The algorithm proposed for the measurement of local pore size with the goal of determining local Knudsen number was shown to be inadequate. A natural next step is to alter the algorithm so that its results match the values provided by the random walk method. Once this is completed, effective diffusivity data using the resulting local Knudsen number must be compared to established diffusivity data to determine if a significant difference exists.

Bibliography

[1] A. Berson, H. W. Choi, and J. G. Pharoah, "Determination of the effective gas diffusivity of a porous composite medium from the three-dimensional reconstruction of its microstructure," *Physical Review E*, vol. 83, 2011.

[2] R. O'Hayre, S. Cha, W. Colella, and F. Prinz, *Fuel Cell Fundamentals.* Wiley and Sons, New York, 2006.

[3] L. L. N. Laboratory, "Solid-oxide fuel cell basics." `https://www.llnl.gov/str/September02/Pham.html`.

[4] S. Singhal and K. Kendall, *High Temperature Solid Oxide Fuel Cells: Fundamentals, Design and Applications.* Elsevier, 2003.

[5] D. A. G. Bruggeman, "Calculation of the various physical constants of heterogeneous substances. dielectric constants and conductivities of mixtures of isotropic substances," *Annual Physik*, vol. 24, pp. 636–664, 1935.

[6] N. Epstein, "On tortuosity and the tortuosity factor in flow and diffusion through porous media," *Chemical Engineering Science*, vol. 44, pp. 777–779, 1989.

[7] H. Moon, S. D. Kim, S. H. Hyun, and H. S. Kim, “Development of it-sofc unit cells with anode-supported thin electrolytes via tape casting and co-firing,” *International Journal of Hydrogen Energy*, vol. 33, pp. 1758–1768, 2008.

[8] J. H. Song, S. I. Park, J. H. Lee, and H. S. Kim, “Fabrication characteristics of an anode-supported thin-film electrolyte fabricated by the tape casting method for it-sofc,” *Journal of Materials Processing Technnology*, vol. 198, pp. 414–418, 2008.

[9] D. Rotureau, J. P. Viricelle, C. Pijolat, N. Caillol, and M. Pijolat, “Development of a planar sofc device using screen-printing technology,” *Journal of European Ceramic Society*, vol. 25, pp. 2633–2636, 2005.

[10] C. Xia, F. Chen, and M. Liu, “Reduced-temperature solid oxide fuel cells fabricated by screen printing,” *Electrochemical and Solid State Letters*, vol. 4, pp. A52–A54, 2001.

[11] Y. Huang, J. M. Vohs, and R. J. Gorte, “Characterization of lsm-ysz composites prepared by impregnation methods,” *Journal of the Electrochemical Society*, vol. 152, pp. A1347–A1353, 2005.

[12] T. Fukui, S. Ohara, M. Naito, and K. Nogi, “Synthesis of nioysz composite particles for an electrode of solid oxide fuel cells by spray pyrolysis,” *Powder Technology*, vol. 132, pp. 52–56, 2003.

[13] R. Hui, Z. Wang, O. Kesler, L. Rose, J. Jankovic, S. Yick, R. Maric, and D. Ghosh, “Thermal plasma spraying for sofcs: Applications, potential advantages, and challenges,” *Journal of Power Sources*, vol. 170, pp. 308–323, 2007.

[14] M. Juhl, S. Primdahl, C. Manon, and M. Mogensen, “Performance/structure correlation for composite sofc cathodes,” *Journal of Power Sources*, vol. 61, pp. 173–181, 1996.

[15] A. Lanzini, P. Leone, and P. Asinari, “Microstructural characterization of solid oxide fuel cell electrodes by image analysis technique,” *Journal of Power Sources*, vol. 194, pp. 408–422, 2009.

[16] N. Shikazono, Y. Sakamoto, Y. Yamaguchi, and N. Kasagi, “Microstructure and polarization characteristics of anode supported tubular solid oxide fuel cell with co-precipitated and mechanically mixed ni-ysz anodes,” *Journal of Power Sources*, vol. 193, pp. 530–540, 2009.

[17] K. Grew, A. Peracchio, J. I. Jr., and W. Chiu, “Nondestructive imaging and analysis of transport processes in the solid oxide fuel cell anode,” *ECS Transactions*, vol. 25, pp. 1861–1870, 2009.

[18] J. R. Izzo, A. S. Joshi, K. N. Grew, W. K. S. Chiu, A. Tkachuk, S. H. Wang, and W. Yun, “Non-destructive reconstruction and analysis of solid oxide fuel cell anodes using x-ray tomography at sub-50 nm resolution,” *ECS Transactions*, vol. 13, pp. 1–11, 2008.

[19] D. Gostovic, J. Smith, D. Kundinger, K. Jones, and E. Wachsman, “Three-dimensional reconstruction of porous lscf cathodes, electrochemical and solid-state letters,” *Electrochemical and Solid-State Letters*, vol. 10, pp. B214–B217, 2007.

[20] H. Iwai, N. Shikazono, T. Matsui, H. Teshima, M. Kishimoto, R. Kishida, D. Hayashi, K. Matsuzaki, D. Kanno, M. Saito, H. Muroyama, K. Eguchi, N. Kasagi, and H. Yoshida, "Quantification of sofc anode microstructure based on dual beam fib-sem technique," *Journal of Power Sources*, vol. 195, pp. 955–961, 2010.

[21] P. Shearing, Q. Cai, J. Golbert, V. Yufit, C. Adjiman, and N. Brandon, "Microstructural analysis of a solid oxide fuel cell anode using focused ion beam techniques coupled with electrochemical simulation," *Journal of Power Sources*, vol. 195, pp. 4804–4810, 2010.

[22] J. Wilson and S. Barnett, "Solid oxide fuel cell ni-ysz anodes: Effect of composition on microstructure and performance," *Electrochemical and Solid-State Letters*, vol. 11, pp. B181–B185, 2008.

[23] J. Wilson, A. Duong, M. Gameiro, H. Chen, K. Thornton, D. Mumm, and S. Barnett, "Quantitative three-dimensional microstructure of a solid oxide fuel cell cathode," *Electrochemistry Communications*, vol. 11, pp. 1052–1056, 2009.

[24] J. Wilson, W. Kobsiriphat, R. Mendoza, H. Chen, T. Hines, J. Hiller, D. Miller, K. Thornton, P. Voorhees, S. Adler, D. Mumm, and S. Barnett, "Three dimensional reconstruction of solid oxide fuel cell electrodes using focused ion beam - scanning electron microscopy," *ECS Transactions*, vol. 7, pp. 1879–1887, 2007.

[25] J. Golbert, C. S. Adjiman, and N. P. Brandon, "Microstructural modeling of solid oxide fuel cell anodes," *Industrial and Engineering Chemistry Research*, vol. 47, pp. 7693–7699, 2008.

[26] D. H. Jeon, J. H. Nam, and C. J. Kim, "A random resistor network analysis on anodic performance enhancement of solid oxide fuel cells by penetrating electrolyte structures," *Journal of Power Sources*, vol. 139, pp. 21–29, 2005.

[27] B. Kenney, M. Valdmanis, C. Baker, J. G. Pharoah, and K. Karan, "Computation of tpb length, surface area and pore size from numerical reconstruction of composite solid oxide fuel cell electrodes," *Journal of Power Sources*, vol. 189, pp. 1051–1059, 2009.

[28] J. H. Nam and D. H. Jeon, "A comprehensive micro-scale model for transport and reaction in intermediate temperature solid oxide fuel cells," *Electrochimica Acta*, vol. 51, pp. 3446–3460, 2006.

[29] B. Kenney and K. Karan, "Impact of nonuniform potential in sofc composite cathodes on the determination of electrochemical kinetic parameters," *Journal of the Electrochemical Society*, vol. 153, pp. A1172–A1180, 2006.

[30] H. W. Choi, A. Berson, J. G. Pharoah, and S. B. Beale, "Effective transport properties of the porous electrodes in solid oxide fuel cells," *Journal of Power and Energy*, vol. 225, pp. 183–197, 2011.

[31] V. P. Schulz, J. Becker, A. Wiegmann, P. P. Mukherjee, and C. Y. Wang, "Modeling of two-phase behavior in the gas diffusion medium of pefcs via full morphology approach," *Journal of the Electrochemical Society*, vol. 154, pp. B419–B426, 2007.

[32] S. H. Kim and H. Pitsch, "Reconstruction and effective transport properties of the catalyst layer in pem fuel cells," *Journal of the Electrochemical Society*, vol. 156, pp. B673–B681, 2009.

[33] P. Levitz, "Knudsen diffusion and excitation transfer in random porous media," *Journal of Physical Chemistry*, vol. 97, pp. 3813–3818, 1993.

[34] J. M. Zalc, S. C. Reyes, and E. Iglesia, "The effects of diffusion mechanism and void structure on transport rates and tortuosity factors in complex porous structures," *Chemical Engineering Science*, vol. 59, pp. 2947–2960, 2004.

[35] O. Ltd., "Openfoam user guide." `http://www.openfoam.com/docs/user/`.

[36] Micromeritics, "Mercury intrusion porosimetry theory." `http://www.micromeritics.com/Repository/Files/Mercury_Porosemitry_Theory_poster_.pdf`.

Appendix A

Additional Figures

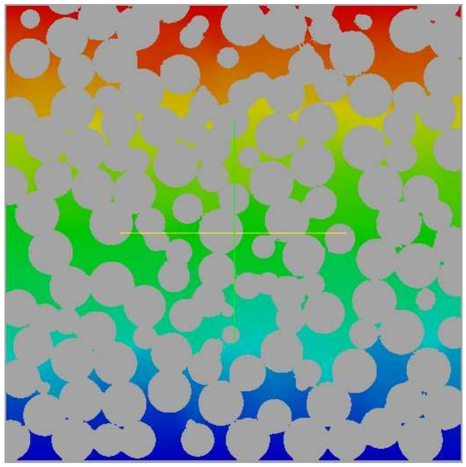

(a) 0 Pore former volume fraction

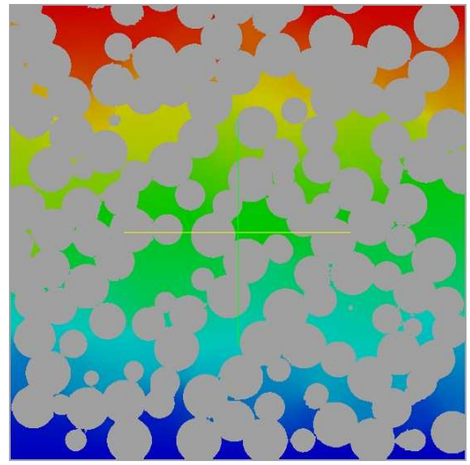

(b) 0.1 Pore former volume fraction

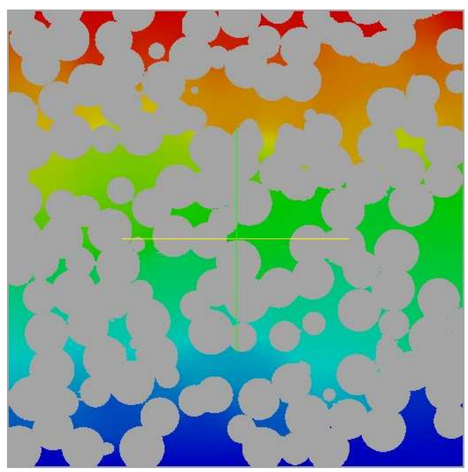

(c) 0.2 Pore former volume fraction

Figure A.1: Extra 2-dimensional slices of the 3D electrode model with varying pore former volume fraction. Porosity for all cases is 35%. The grey area represents both the ion and electron conducting phases, while the pore space is represented by a concentration gradient.

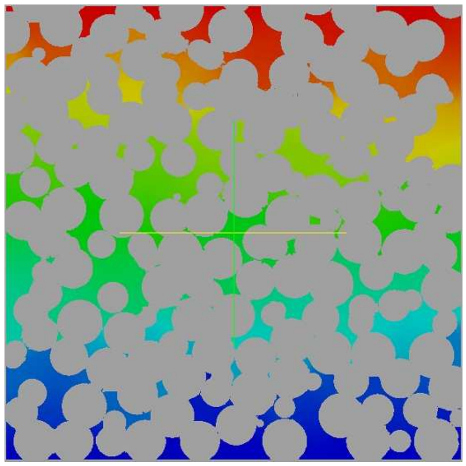

(a) 0 Pore former volume fraction, 25% porosity

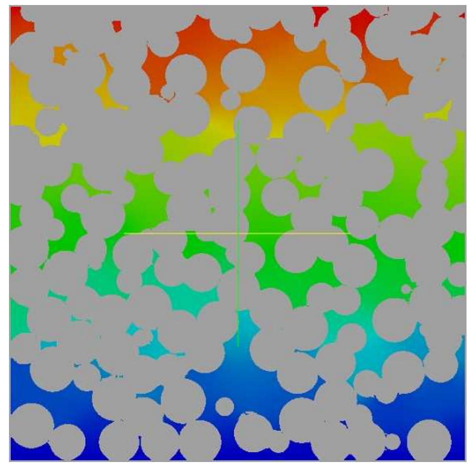

(b) 0.1 Pore former volume fraction, 32% porosity

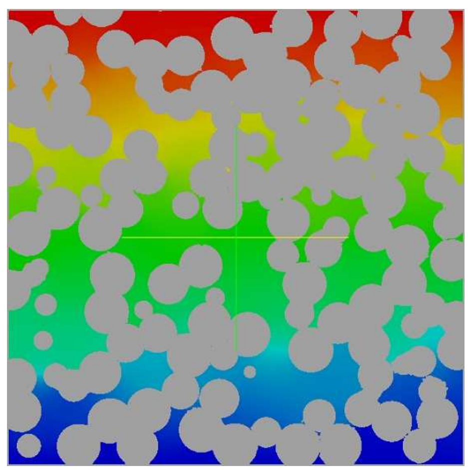

(c) 0.2 Pore former volume fraction, 39% porosity

Figure A.2: Extra 2-dimensional slices of the 3D electrode model with varying pore former volume fraction and constant particle overlap. The grey area represents both the ion and electron conducting phases, while the pore space is represented by a concentration gradient.

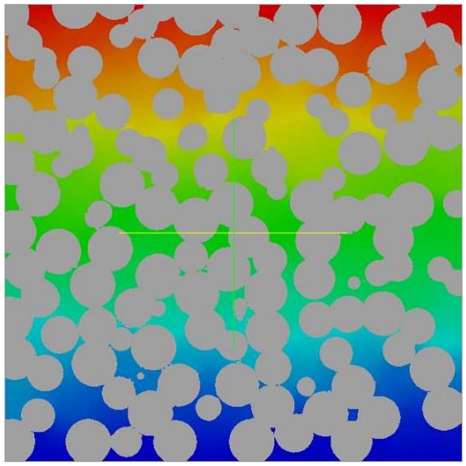

(a) 0.036 Pore former particle size

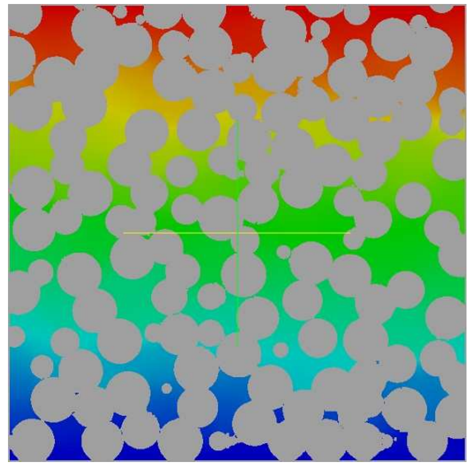

(b) 0.062 Pore former particle size

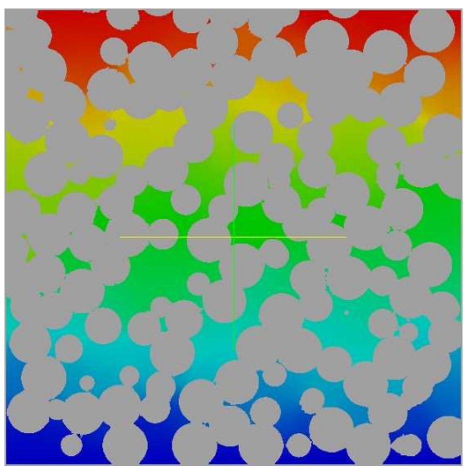

(c) 0.1 Pore former particle size

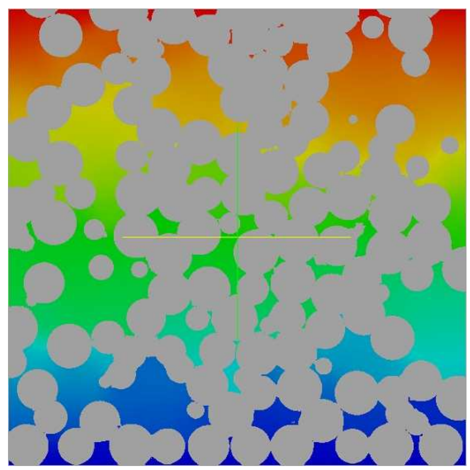

(d) 0.16 Pore former particle size

Figure A.3: Extra 2-dimensional slices of the 3D electrode model with varying pore former particle size. Porosity for both cases is 35% and pore former volume fraction is 0.1. The grey area represents both the ion and electron conducting phases, while the pore space is represented by a concentration gradient.

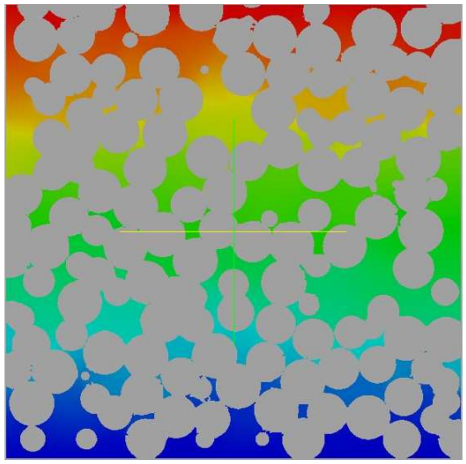

(a) Two single sphere phases

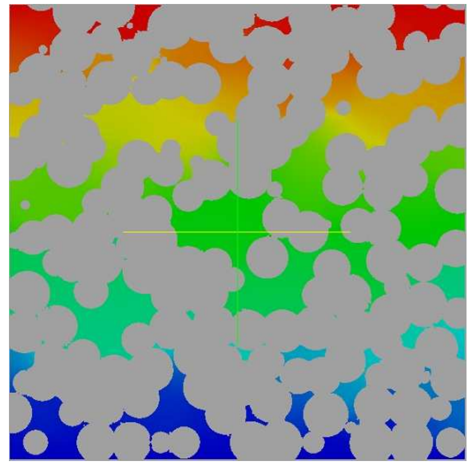

(b) One pre-agglomerated phase

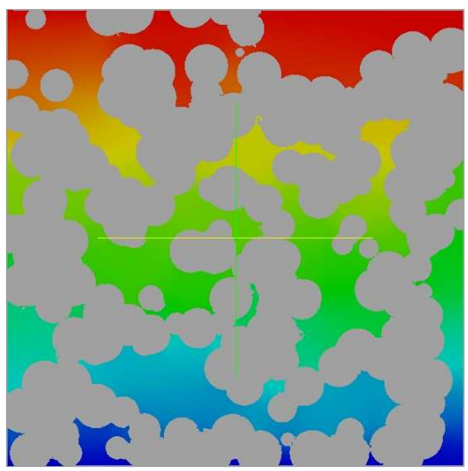

(c) Two pre-agglomerated phases

Figure A.4: Extra 2-dimensional slices of the 3D electrode model with various levels of pre-agglomeration. Porosity for both cases is 30%. The grey area represents both the ion and electron conducting phases, while the pore space is represented by a concentration gradient.

Appendix B

Additional Analysis

B.1 FVM Diffusivity Results

The following tables display quantitative results for effective diffusivity using an FVM technique and the CFD program OpenFOAM. The effective diffusivity results using FVM display the same trends discovered while using the random walk routine.

Table B.1: Effective diffusivity for several values of pore former volume fraction using FVM.

Pore Former Volume Fraction	0	0.1	0.2
De/Db - constant porosity	0.181	0.170	0.173
De/Db - constant particle overlap	0.094	0.137	0.205

Table B.2: Effective diffusivity for several values of pore former particle size using FVM.

Pore Former Particle Size	0.036	0.062	0.100	0.160
De/Db	0.184	0.176	0.170	0.167

Table B.3: Effective diffusivity for a varying number of pre-agglomerated phases using FVM.

Pore Former Particle Size	No phases	One phase	Two Phases
De/Db	0.137	0.117	0.135